Geomechanical property estimation of unconventional reservoirs using seismic data and rock physics

Michael E. Glinsky[1]*, Andrea Cortis[2], Jinsong Chen[4], Doug Sassen[3] and Howard Rael[3]

[1]*Geotrace Technologies, 12141 Wickchester Lane, Suite 200, Houston, TX, 77079*, [2]*AYASDI, 4400 Bohannon Dr., Suite 200, Menlo Park, CA, 94025*, [3]*ION Geophysical, 2105 CityWest Blvd., Suite 900, Houston, TX, 77042, and* [4]*Lawrence Berkeley National Laboratory, 1 Cyclotron Road, Berkeley, CA 94720*

ABSTRACT

An extension of a previously developed rock physics model is made that quantifies the relationship between the ductile fraction of a brittle/ductile binary mixture and the isotropic seismic reflection response. By making a weak scattering (Born) approximation and plane wave (eikonal) approximation, with a subsequent ordering according to the angles of incidence, singular value decomposition analyses are performed to understand the stack weightings, number of stacks, and the type of stacks that will optimally estimate two fundamental rock physics parameters – the ductile fraction and the compaction and/or diagenesis. It is concluded that the full PP stack, i.e., sum of all PP offset traces, and the "full" PS stack, i.e., linear weighted sum of PS offset traces, are the two optimal stacks needed to estimate the two rock physics parameters. They dominate over both the second-order amplitude variation offset "gradient" stack, which is a quadratically weighted sum of PP offset traces that is effectively the far offset traces minus the near offset traces, and the higher order fourth order PP stack (even at large angles of incidence). Using this result and model-based Bayesian inversion, the seismic detectability of the ductile fraction (shown by others to be the important rock property for the geomechanical response of unconventional reservoir fracking) is demonstrated on a model characteristic of the Marcellus shale play.

Key words: Quantitative interpretation, Rock physics, Seismics, Multi-component, Unconventional reservoir, Inverse problem.

INTRODUCTION

Ductile fraction is one of the two important order parameters for the linear, isotropic, elastic response of binary mixtures of a structurally competent member (high coordination number) and a structurally less competent member (lower coordination number). A very important implication of this bi-critical model is that the state is only two dimensional. The expectation and practical reality (as demonstrated by analysis of well log data) is that the isotropic properties will reduce to a surface in the 3D density, compressional velocity, and shear velocity (i.e., ρ, v_p, v_s) space. Furthermore, this surface will be orthogonal to the v_p–v_s plane. The remarkable property of the reduction in dimension is captured by the floating grain model (Demartini and Glinsky 2006; Gunning and Glinsky 2007), which has two state variables given by the floating grain fraction f_f and the compaction state as specified by $1 - \exp(-P_e/P_0)$, where P_e is the effective stress and P_0 is a reference value of effective stress. Two phase transitions points at critical values in the radius ratio (at $RR_c = 4$) and the fraction of small grains (at $VF_c = 0.45$) were demonstrated, as well as two critical scalings of the porosity about a critical point of about 42% by Bryant, Lerch, and Glinsky (2009).

*E-mail: glinsky@qitech.biz

The floating grain theory was developed for a binary mixture of brittle spheres of two different sizes. Recognizing that the large spheres are the structurally competent member and the small spheres are the structurally less competent member, we generalize the floating grain theory in the Rock physics Section. The floating grain fraction is replaced by a general geometry parameter ξ, which in the case of shales is shown to be proportional to f_d, where f_d is the ductile fraction. The geometry parameter captures the fabric of the mixture such as the sorting or ductile fraction, whereas the composition parameter captures the compaction, diagenesis, and/or mineral substitution of the mixture. An important additional implication of the bicritical model is a fundamental self-similarity and the associated scaling relationships (Stauffer and Aharony 1994) of physical quantities such as coordination numbers, capture fractions, and elastic moduli. It also implies the same critical scaling for both v_p and v_s because they have the same units. Therefore the surface in (ρ, v_p, v_s) space should be orthogonal to the v_p–v_s plane.

The rock physics and geophysical detectability of the fracability of unconventional reservoirs has been, and continues to be, a very active area of research. Hornby, Schwartz and Hudson (1994) developed an anisotropic effective media model for the elastic properties of shales. The use of converted wave seismic data in the exploration of unconventional reservoirs was discussed by Stewart *et al.* (2002). The inversion of PP and PS data for geophysical properties was discussed by Mahmoudian and Margrave (2004) and Veire and Landr (2006). There is a good discussion of the rock physics of shales focusing on the anisotropy by Sayers (2005). Goodway *et al.* (2010), Sayers (2013), Vernik and Kachanov (2010) and Khadeeva and Vernik (2013) are well cited references that present petrophysical models for shales that have an AVO expression. Finally, a shale rock physics model for the analysis of brittleness was developed by Guo *et al.* (2013).

The developing commercial significance of unconventional shale reservoirs leads to the need of remotely determining the ability to effectively fracture the reservoir. This paper will establish the theory and practicality of optimally estimating the ductile fraction from an isotropic analysis of surface conventional and converted wave seismic data. Ductile fraction is defined as the ratio of the structurally incompetent (ductile) organic matter (total organic carbon, TOC) and clay, to the sum of the structurally incompetent plus the structurally competent (brittle) quartz and calcium carbonate by volume. Structural competence comes from having a larger coordination number or, equivalently, from having more elastic moduli per mass. The ductile fraction of a binary ductile/brittle mixture has been shown to be the key property in determining the geomechanical fracturing response of an unconventional reservoir (Zoback *et al.* 2012; Kohli and Zoback 2013). The importance of the ductile fraction is, most likely, because of the balance between the "bumpy road" friction of the fracture, due to the structurally competent brittle member, and the viscous friction, due to the ductile member. The detailed mechanism is not the subject of this paper but is the topic of our ongoing research into the statistical mechanics of fracture joint friction.

We emphasize the serendipity of the fact that the ductile fraction is the coordinate of influence of both the linear elastic response (geophysical) and the nonlinear inelastic response (geomechanical). For the former, the ductile material is adding density without much structural rigidity, i.e., elastic moduli. For the latter, it is increasing the importance of the viscous joint friction.

Before continuing, a few words need to be said about focusing on the isotropic response of the shale. It is well known that there are both strong vertical transverse anisotropy, caused by the depositional lamination, and horizontally transverse anisotropy, caused by post-depositional vertical fractures. We are not ignoring that the rocks are anisotropic, but we are rather separating the problem into the diagonal isotropic part and the off-diagonal anisotropic part. The analysis of this paper shows that there are two directionally averaged coordination numbers that are characterized by two scalars that characterize the geometry and the composition. The geometry is characterized by the scalar ductile fraction. It is expected that the anisotropy will characterize the vertical fracture density and orientation, as well as the degree of horizontal lamination. The additional information that comes from the anisotropy is important information that affects the geomechanical response, complementary to the ductile fraction. However, extension of this theory to include anisotropy is the topic of our ongoing research.

Given the ductile fraction rock physics model, this paper examines its implication on the geophysical detectability of ductile fraction in the Applications Section. Several questions have been the subject of much debate within the geophysical community (see the references of the previous paragraph). For example, how many stacks should be used in "pre-stack" analysis? What should those stacks be? What is the relative value of amplitude variation offset (AVO) versus converted wave data analysis? What is the value of determining density from large-angle PP data? What are the quantities that should be inverted for, relative (reflectivity) versus absolute (impedance)? Finally, what are the "attributes" that best predict reservoir performance?

We present a straightforward analytic theory in the Singular value decomposition theory Section and subsequent analysis that answers all of these questions in the Detectability without rock physics uncertainty Section. It is a linear singular value decomposition analysis (Saleh and de Bruin 2000; Causse *et al.* 2007a, 2007b; Varela *et al.* 2009) of the relationship between the two fundamental rock physics parameters (ζ, which is the composition, and ξ, which is the geometry, to be defined more precisely in the succeeding Rock physics Section) and the seismic reflectivities (PP and PS) as functions of angle of incidence θ. This analysis is done by assuming a weak scattering (Born) approximation and plane wave assumption (eikonal). It also orders the SVD using the angle θ. It should be noted that the SVD analysis is facilitated by a novel expansion and simplification of the geophysical forward model shown in Appendix A. Distortions caused by angle-dependent noise and by angle-dependent multiplicative factors are examined in Appendix B.

Finally, the practical seismic detectability, on a synthetic example based on the Marcellus shale play, is shown in the Applications Section. There are many factors that can complicate and confound this analysis, such as tuning effects of multiple layers, low SNR in real data, and uncertainty in the rock physics model. To address these issues on a prototypical example, a principle components analysis and wavelet derivation on real data are done in the Appendix C. This includes stack weight profiles, spectral SNR analysis, and wavelet profiles. The uncertainty of the rock physics model is estimated using reasonably large well-log database from several unconventional shale plays. First, the SVD analysis is extended to include the rock physics uncertainty in the Detectability with rock physics uncertainty Section, and the detectability of the rock physics parameters ζ and ξ is determined. Second, it is used to construct a layer-based model of the Marcellus play with uncertainty (in the Marcellus prototype model Section), to forward model the synthetic and finally to do a layer-based Bayesian inversion (Gunning and Glinsky 2004; Chen and Glinsky 2014) of this model (in the Model based inversion Section). Very good sensitivity to the ductile fraction is found in the high TOC (Total Organic Carbon) shale layers. Significant additional sensitivity is found by using the "full" PS data, in addition to the full PP data.

THEORY

Rock physics

We first recognize that we are dealing with a binary mixture of a ductile member and a brittle member, where the latter is more structurally competent than the former. We take inspiration from the floating grain model (Demartini and Glinsky 2006). This model is based on two fundamental parameters – the floating grain fraction parameterized by $\xi = f_f/f_{fc}$ and the compaction parameterized by $\zeta = 1 - \exp(-P_e/P_0)$, where f_f is the floating grain fraction, f_{fc} is the maximum or critical floating grain fraction, P_e is the effective stress, and P_0 is a reference effective stress. The model respects fluid substitution and leads to local linear correlations of the form

$$v_p = A_{vp} + B_{vp}\,\zeta + C_{vp}\,\xi \;\pm \sigma_{vp}, \tag{1}$$

$$\phi = A_\phi + B_\phi\,v_p + C_\phi\,\xi \;\pm \sigma_\phi, \text{ and} \tag{2}$$

$$v_s = A_{vs} + B_{vs}\,v_p \;\pm \sigma_{vs}. \tag{3}$$

The second relationship can be rewritten in two ways, given ρ_s and ρ_f and the definition $\rho \equiv \phi\,\rho_f + (1-\phi)\rho_s$, as follows:

$$\phi = \phi_c - \frac{\phi_c}{n_\zeta}\,\zeta - \frac{\phi_c}{n_\xi}\,\xi, \text{ and} \tag{4}$$

$$\rho = A_\rho + B_\rho\,v_p + C_\rho\,\xi \;\pm \sigma_\rho. \tag{5}$$

Equation (4) identifies the two critical exponents n_ζ and n_ξ, and the critical porosity ϕ_c in the linear expansion as $\phi/\phi_c \to 0$ of the following expressions for the critical scalings of ζ and ξ, respectively:

$$\zeta \sim \left(\frac{\phi_c - \phi}{\phi_c}\right)^{n_\zeta} \text{ and } \xi \sim \left(\frac{\phi_c - \phi}{\phi_c}\right)^{n_\xi}. \tag{6}$$

Equation (5) is just a convenient expression to compare with the log data of shales.

For the rocks studied by Demartini and Glinsky (2006), the regressed values are given by $A_{vp} = 1524$ m/s, $B_{vp} = 2050$ m/s, $C_{vp} = 490$ m/s, $\sigma_{vp} = 107$ m/s, $A_\phi = 0.592$, $B_\phi = -1.03 \times 10^{-4}$ s/m, $C_\phi = -0.0878$, $\sigma_\phi = 0.0093$, $A_{vs} = -884$ m/s, $B_{vs} = 0.894$, $\sigma_{vs} = 69$ m/s, $\phi_c = 0.435$, $n_\zeta = 2.06$, $n_\xi = 3.11$, $P_0 = 8.89$ MPa, $f_{fc} = 0.09$, $A_\rho = 1.69$ g/cc, $B_\rho = 1.75 \times 10^{-4}$ (s/m)(g/cc), $C_\rho = 0.149$ g/cc, and $\sigma_\rho = 0.016$ g/cc. We have assumed $\rho_s = 2.7$ g/cc and $\rho_f = 1.0$ g/cc in these relationships. Note that ϕ_c is the expected percolation threshold. A very important property of this model is the form of the v_s correlation – it is only a function of v_p and does not involve either ζ or ξ. This means that the rock physics correlates the ρ, v_p, and v_s values into a plane that is orthogonal to the v_p–v_s plane. Characteristic values for the rock physics parameters are $\zeta = 0.910 \pm 0.012$ and $\xi = 0.22 \pm 0.33$.
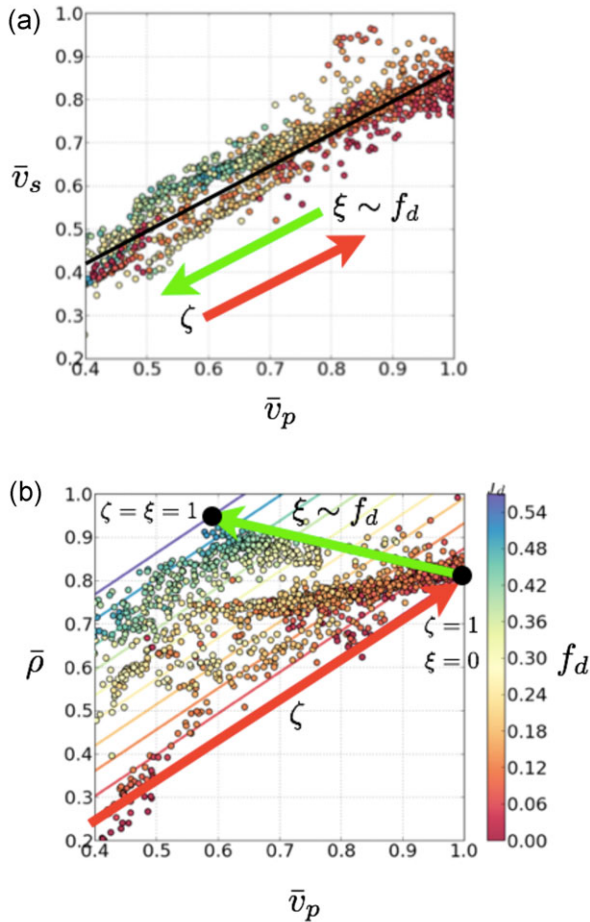
Figure 1 Well log data supporting rock physics model. Points are blocked well-log data coloured according to the ductile fraction f_d. Also shown are the directions of increasing ζ (constant ξ) as the red arrow and increasing ξ (constant ζ) as the green arrow. Values are normalized according to the equation $\bar{x} = (x - x_{min})/(x_{max} - x_{min})$, where min $v_p = 2439$ m/s, max $v_p = 5488$ m/s, min $v_s = 1158$ m/s, max $v_s = 3354$ m/s, min $\rho = 2.1$ g/cc, and max $\rho = 2.8$ g/cc. (a) v_s-v_p trend in normalized units. Black line is the fit trend, equation (3). (b) ρ-v_p trend in normalized units. Trend lines of constant ξ, equation (1), are colored according to the value of $f_d = f_{dc}\xi$. The two end members for fully compacted ductile and brittle rocks are shown as black dots.

When we examine shales from many different wells and plays, we get the results shown in Fig. 1. It is important to note the strong linear correlation in the v_p–v_s plane of Fig. 1a and the systematic shift in the ρ-v_p correlation with the ductile fraction f_d in Fig. 1b. Inspired by the floating grain model, we generalize ξ to f_d/f_{dc}, where f_d is the ductile fraction, and f_{dc} is the maximum or critical ductile fraction. Given the range of the data, the line in Fig. 1b shows the variation in the ρ-v_p as ξ

goes from 0 to 1 for $\zeta = 1$, and we assume that the minimum value of v_p is 2896 m/s when $\zeta = \xi = 0$. A regression to this extended rock physics model leads to $A_{vp} = 2896$ m/s, $B_{vp} = 2591$ m/s, $C_{vp} = -1372$ m/s, $\sigma_{vp} = 107$ m/s, $A_\phi = 0.771$, $B_\phi = -1.21 \times 10^{-4}$ s/m, $C_\phi = -0.1916$, $\sigma_\phi = 0.017$, $A_{vs} = 390$ m/s, $B_{vs} = 0.48$, $\sigma_{vs} = 66$ m/s, $\phi_c = 0.421$, $n_\zeta = 1.34$, $n_\xi = 16.4$, $f_{dc} = 0.52$, $A_\rho = 1.435$ g/cc, $B_\rho = 2.30 \times 10^{-4}$ (s/m)(g/cc), $C_\rho = 0.364$ g/cc, and $\sigma_\rho = 0.032$ g/cc. We have assumed $\rho_s = 2.9$ g/cc and $\rho_f = 1.0$ g/cc in these relationships. We note that there was a four-fold decrease in σ_ρ by including the C_ρ term in the regression of the data sets. Note the reasonable value of ϕ_c. The self similarity of the rock structure implied by this model is validated by neutron scattering experiments (Clarkson *et al.* 2013), which shows a distinct power law behavior in the pore size distribution. Characteristic values of the rock physics parameters are $\zeta = 0.75 \pm 0.07$ and $\xi = 0.70 \pm 0.20$. Straightforward analysis shows that the capture fraction, as defined by Demartini and Glinsky (2006), scales as $n_\xi/(n_\xi - n_\zeta)$, is approximately equal to the reciprocal of this exponent for states away from the critical point, and is the ratio of the ductile coordination number to the brittle coordination number. This gives a capture fraction of 92% for this model and 36% for the floating grain work of Demartini and Glinsky (2006).

We have not explicitly identified the process and therefore the "activation energy" in the definition of $\zeta \equiv 1 - \exp(-E/E_0)$. Unlike for the floating grain model, changes in the composition are not limited to compaction (there is probably a very large amount of diagenesis and mineral substitution for shales), and we did not have information on what the controlling variables (i.e., effective stress or temperature) were for each of the well-log samples. Practically, this is not a limitation since we are not trying to estimate the energy E and that value will be assumed a constant for a stratigraphic layer in our analysis. With this notwithstanding, there is a strong possibility that if the compaction and diagenesis are constant for a stratigraphic interval, the composition variable would be diagnostic of the organic matter (TOC) to clay ratio.

The relationship for the shift in the ρ versus v_p trend, given equation (5), or equivalently the ϕ versus v_p trend, given by equation (2), with clay fraction has also been noted by Han, Nur, and Morgan (1986) and Pervukhina *et al.* (2013) in laboratory core data.

Singular value decomposition (SVD) theory

We now move onto understanding the relationships between the basic rock physics parameters that we wish to know, i.e., ξ and ζ, and the geophysical measurements. We do this by

establishing a sequence of linear transformations, then examining the important singular value decompositions (SVDs) of that compound transformation. The singular values will give an understanding of detectability of the singular vectors (i.e., the required SNR). The singular vectors will tell us what views of the measurement to use and how they are related to the rock physics.

We start by writing the expression for the measured reflectivity in the following linear form

$$\mathbf{R}_m = \mathbf{DM}_\theta(\mathbf{M}_A(\mathbf{M}_{RP}\Delta\mathbf{r} + \boldsymbol{\varepsilon}_r) + \boldsymbol{\varepsilon}_A) + \boldsymbol{\varepsilon}_m, \tag{7}$$

where $\mathbf{R}_m$ is the measured value of $\mathbf{R}$, $\mathbf{D}$ is a linear distortion of the measurement of $\mathbf{R}$, $\mathbf{M}_\theta$ is the angle matrix, $\mathbf{M}_A$ is the geophysical reflection matrix, $\mathbf{M}_{RP}$ is the rock physics matrix, $\Delta\mathbf{r}$ is the change in the rock physics parameters, $\boldsymbol{\varepsilon}_r$ is the error vector in the rock physics relationships, $\boldsymbol{\varepsilon}_A$ is the error vector in the geophysical forward model, and $\boldsymbol{\varepsilon}_m$ is the error vector in the measurement of $\mathbf{R}$. For the detailed definitions of these matrices, see Appendix A. By re-organizing equation (7), we get

$$\mathbf{R}_m = \mathbf{DM}_\theta\mathbf{M}_A\mathbf{M}_{RP}\Delta\mathbf{r} + \mathbf{D}(\mathbf{M}_\theta\mathbf{M}_A\boldsymbol{\varepsilon}_r + \mathbf{M}_\theta\boldsymbol{\varepsilon}_A) + \boldsymbol{\varepsilon}_m \tag{8}$$

$$= \mathbf{R}_0 + \boldsymbol{\varepsilon}_c. \tag{9}$$

Here $\mathbf{R}_0$ are the most likely reflection coefficients, i.e.,

$$\mathbf{R}_0 \equiv \mathbf{DM}_\theta\mathbf{M}_A\mathbf{M}_{RP}\Delta\mathbf{r}, \tag{10}$$

and $\boldsymbol{\varepsilon}_c$ is combined error in the estimate of the reflection coefficients, i.e.,

$$\boldsymbol{\varepsilon}_c \equiv \mathbf{D}(\mathbf{M}_\theta\mathbf{M}_A\boldsymbol{\varepsilon}_r + \mathbf{M}_\theta\boldsymbol{\varepsilon}_A) + \boldsymbol{\varepsilon}_m. \tag{11}$$

Assume that the expected values of the fundamental errors of $\boldsymbol{\varepsilon}_r$, $\boldsymbol{\varepsilon}_A$, and $\boldsymbol{\varepsilon}_m$ are 0; the covariances are given by $\boldsymbol{\Sigma}_r$, $\boldsymbol{\Sigma}_A$, and $\boldsymbol{\Sigma}_m$ respectively; and that $\boldsymbol{\varepsilon}_r$, $\boldsymbol{\varepsilon}_A$, and $\boldsymbol{\varepsilon}_m$ are independent and normally distributed. It follows that expected value $\boldsymbol{\varepsilon}_c$ is 0, and the covariance is given by

$$\boldsymbol{\Sigma}_c = \boldsymbol{\Sigma}_m + (\mathbf{DM}_\theta)\boldsymbol{\Sigma}_A(\mathbf{DM}_\theta)^T + (\mathbf{DM}_\theta\mathbf{M}_A)\boldsymbol{\Sigma}_r(\mathbf{DM}_\theta\mathbf{M}_A)^T. \tag{12}$$

In other words, the measurement of the reflection coefficients is distributed according to a multivariant normal distribution MVN($\mathbf{R}_0$, $\boldsymbol{\Sigma}_c$), with a probability density given by

$$P(\mathbf{R}_m) \sim \exp\left\{-\frac{1}{2}(\mathbf{R}_m - \mathbf{R}_0)^T\boldsymbol{\Sigma}_c^{-1}(\mathbf{R}_m - \mathbf{R}_0)\right\} \tag{13}$$

With these definitions now in hand, we return to the form of the distribution for $\mathbf{R}_m$ given in equation (13). Since $\boldsymbol{\Sigma}_c$ is positive definite, it can be written as

$$\boldsymbol{\Sigma}_c^{-1} = \mathbf{W}_d^T\mathbf{W}_d. \tag{14}$$

We make two singular value decompositions (SVDs) such that

$$\mathbf{W}_d\mathbf{DM}_\theta = \mathbf{U}_1\boldsymbol{\Sigma}_1\mathbf{V}_1^T \tag{15}$$

and

$$\overline{\boldsymbol{\Sigma}}_1\mathbf{V}_1^T\mathbf{M}_A\mathbf{M}_{RP} = \mathbf{U}_2\boldsymbol{\Sigma}_2\mathbf{V}_2^T. \tag{16}$$

We define $\overline{\boldsymbol{\Sigma}}_1$ and $\overline{\boldsymbol{\Sigma}}_2$ as the square diagnal matrices formed by dropping the zero rows of $\boldsymbol{\Sigma}_1$ and $\boldsymbol{\Sigma}_2$, respectively. We also define $\overline{\mathbf{U}}_1$ and $\overline{\mathbf{U}}_2$ by dropping the corresponding columns of $\mathbf{U}_1$ and $\mathbf{U}_2$, respectively.

First of all, write the distribution as

$$P(\mathbf{R}_m) \sim \exp\left\{-\frac{1}{2}(\mathbf{W}_d\mathbf{R}_m - \mathbf{W}_d\mathbf{R}_0)^T(\mathbf{W}_d\mathbf{R}_m - \mathbf{W}_d\mathbf{R}_0)\right\} \tag{17}$$

$$\sim \exp\left\{-\frac{1}{2}\boldsymbol{\chi}^T\boldsymbol{\chi}\right\}, \tag{18}$$

where

$$\boldsymbol{\chi} \equiv \mathbf{W}_d\mathbf{R}_m - \mathbf{W}_d\mathbf{DM}_\theta\mathbf{M}_A\mathbf{M}_{RP}\Delta\mathbf{r}. \tag{19}$$

Now make the change of coordinates such that

$$\boldsymbol{\chi}^* \equiv \overline{\mathbf{U}}_2^T\overline{\mathbf{U}}_1^T\boldsymbol{\chi}. \tag{20}$$

Using these definitions, it can be shown that

$$\boldsymbol{\chi}^T\boldsymbol{\chi} = (\boldsymbol{\chi}^*)^T\boldsymbol{\chi}^* + H \tag{21}$$

where H is not a function of $\Delta\mathbf{r}$ (thus, it does not affect the likelihood function of $\Delta\mathbf{r}$) and

$$\boldsymbol{\chi}^* = \overline{\mathbf{U}}_2^T(\overline{\mathbf{U}}_1^T\mathbf{W}_d)\mathbf{R}_m - \overline{\boldsymbol{\Sigma}}_2\mathbf{V}_2^T\Delta\mathbf{r} \tag{22}$$

$$= (\overline{\boldsymbol{\Sigma}}_2\mathbf{V}_2^T)[\Delta\mathbf{r}_0 - \Delta\mathbf{r}], \tag{23}$$

where we define

$$\Delta\mathbf{r}_0 \equiv (\overline{\boldsymbol{\Sigma}}_2\mathbf{V}_2^T)^{-1}\overline{\mathbf{U}}_2^T(\overline{\mathbf{U}}_1^T\mathbf{W}_d)\mathbf{R}_m \tag{24}$$

and let

$$\boldsymbol{\Sigma}_{\Delta\mathbf{r}}^{-1} \equiv (\overline{\boldsymbol{\Sigma}}_2\mathbf{V}_2^T)^T(\overline{\boldsymbol{\Sigma}}_2\mathbf{V}_2^T). \tag{25}$$

Given that $\mathbf{R}_m$ is the observed forward-modelled reflection response of rock properties $\mathbf{r}_1$ over $\mathbf{r}_0$, such that $\Delta\mathbf{r}_0 = \mathbf{r}_1 - \mathbf{r}_0$ and $\Delta\mathbf{r} = \mathbf{r} - \mathbf{r}_0$, the probability of $\mathbf{r}$ can be written as the multivariate normal distribution MVN($\Delta\mathbf{r}_0$, $\boldsymbol{\Sigma}_{\Delta\mathbf{r}}$), with a probability of $\mathbf{r}$ given by

$$P(\mathbf{r}) \sim \exp\left\{-\frac{1}{2}(\mathbf{r} - \mathbf{r}_1)\boldsymbol{\Sigma}_{\Delta\mathbf{r}}^{-1}(\mathbf{r} - \mathbf{r}_1)\right\}. \tag{26}$$

Let us now make some practical identifications. First, recognize that $\overline{\mathbf{U}}_1^T\mathbf{W}_d$ transforms $\mathbf{R}_m$ into m "stacks", where

m is the dimension of the A matrix (either 3, 5, or 6, for equation (A28), (A29) or (A30), respectively). We will denote these stacks as R_i so

$$\tilde{\mathbf{R}} \equiv \begin{pmatrix} R_0 \\ R_1 \\ \vdots \\ R_{m-1} \end{pmatrix}, \text{ and } \overline{\boldsymbol{\Sigma}}_1 = \begin{pmatrix} \lambda_0 & 0 & 0 & 0 \\ 0 & \lambda_1 & 0 & 0 \\ 0 & 0 & \ddots & 0 \\ 0 & 0 & 0 & \lambda_{m-1} \end{pmatrix}. \quad (27)$$

The signal-to-noise ratio (SNR) of the stack R_i is defined as $20 \log_{10} \lambda_i$, and $\lambda_i \sim \theta_m^i$. $\mathbf{V}_2^T$ is a 2×2 matrix that rotates $\Delta \mathbf{r}$ so that they are orthogonal, i.e., $\Delta \tilde{\mathbf{r}} = \mathbf{V}_2^T \Delta \mathbf{r}$. Then the m stacks $\tilde{\mathbf{R}}$ are projected by $\overline{\mathbf{U}}_2^T$ (a $2 \times m$ matrix) onto the two orthogonal rock physics directions. The two singular values given by the diagonal matrix $\overline{\boldsymbol{\Sigma}}_2$ give the uncertainty of the estimates of the rock physics parameters along the two orthogonal directions in the rock physics space $\Delta \tilde{\mathbf{r}}$ defined by $\mathbf{V}_2^T$. One can directly form the two optimal stacks for estimation of the two orthogonal rock physics parameters $\tilde{\zeta}$ and $\tilde{\xi}$ by $\overline{\mathbf{U}}_2^T \overline{\mathbf{U}}_1^T \mathbf{W}_d$.

Many of the current inversion schemes invert for various moduli and other elastic parameters such as densities and Poisson ratios. There have been historical debates on which of these combinations are best to estimate the fundamental rock physics parameters that continue to this day. It is our view that this is an irrelevant debate. The relevant question is what are the orthogonal stacks of the data covariance matrix with positive SNR and how are they related to the orthogonal coordinates of the rock physics. Notwithstanding this point, there is something to be learned from examining the linear mapping of the rock physics to contrasts in these traditional variables and the SVD of that transformation.

We start this analysis with the definition of a reasonably representative set of traditional parameters that consists of the shear modulus,

$$G \equiv \rho \, v_s^2, \quad (28a)$$

the bulk modulus,

$$K \equiv \rho \, v_p^2 - \frac{4}{3} G, \quad (28b)$$

the Young's modulus,

$$E \equiv \frac{9KG}{3K + G}, \quad (28c)$$

the Poisson ratio,

$$\nu \equiv \frac{3K - 2G}{2(3K + G)}, \quad (28d)$$

the v_p-to-v_s ratio,

$$r_{ps} \equiv v_p / v_s, \quad (28e)$$

and the density ρ.

Using equation (A32) and (A27), we write

$$\Delta \mathbf{r}_T = \mathbf{M}_T \mathbf{M}_{RP} \Delta \mathbf{r}. \quad (29)$$

Now make the SVD, so that $\mathbf{M}_T \mathbf{M}_{RP} = \mathbf{U}_T \boldsymbol{\Sigma}_T \mathbf{V}_T^T$. The $\mathbf{V}_T = \mathbf{V}_2$ that we found before; therefore, we write

$$\overline{\mathbf{U}}_T^T \Delta \mathbf{r}_T = \overline{\boldsymbol{\Sigma}}_T \mathbf{V}_2^T \Delta \mathbf{r} = \overline{\boldsymbol{\Sigma}}_T \Delta \tilde{\mathbf{r}}. \quad (30)$$

The interesting part of this SVD is $\overline{\mathbf{U}}_T^T$, which is a 2×6 matrix that projects the traditional rock physics contrasts onto two orthogonal rock physics directions.

APPLICATIONS

Detectability without rock physics uncertainty

This is still abstract at this point. Let us substitute in the rock physics of the shales given in the latter part of the Rock physics Section. For now we set the multiplicative distortion $\mathbf{D}$ to the identity matrix and the data covariance $\boldsymbol{\Sigma}_m$ to a diagonal constant of 1. We shall return to this in Appendix B. We also ignore errors in rock physics and in the forward model at this stage. As a result, we can drop $\boldsymbol{\Sigma}_r$ and $\boldsymbol{\Sigma}_A$ in the equations. We shall return to the implications of rock physics uncertainty on the detectability of ductile fraction in the Detectability with rock physics uncertainty Section. The matrix $\mathbf{W}_d$ will therefore be the identity matrix. We set the rock physics composition to $\zeta = 0.79$ and the geometry to $\xi = 0.5$. This gives a density of $\rho = 2.59$ g/cc, compressional velocity of $v_p = 4268$ m/s, a shear velocity of $v_s = 2439$ m/s, a v_p-to-v_s ratio of $\mathbf{r}_{ps} = 1.75$, a Poisson ratio of $\nu = 0.26$, and a porosity of $\phi = 16\%$.

For a small maximum angle of $\theta_m = 0.5°$, we get the stack weights $\overline{\mathbf{U}}_1^T$ shown in Fig. 2. We have shown the results for the six-term A vector, but the other two are just truncated versions of this result. It should be noted that this result is independent of that of the rock physics, i.e., $\mathbf{M}_{RP}$, and the relationship between the rock physics and the A's i.e., $\mathbf{M}_A$. In the order of decreasing singular value, or SNR, we have R_0 for the full PP stack, R_1 for the "full" PS stack (in quotes because it is really linearly weighted with θ), and R_2 for the AVO PP gradient stack (weighted by θ^2 so that it is the far offsets minus the near offsets). The series continues on with progressively higher θ order weightings of the stacks in an alternating order between the PP and the PS data. The next figure (Fig. 3) shows the dependance of the singular values on
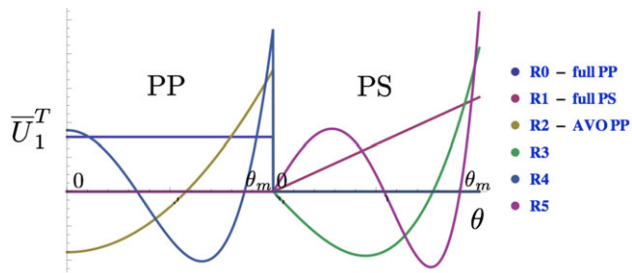
Figure 2 Stack weights, $\overline{U}_1^T$, as a function of incidence angle θ. First set is for PP data, followed by the weights for PS data. The maximum angle θ_m is 0.5°.
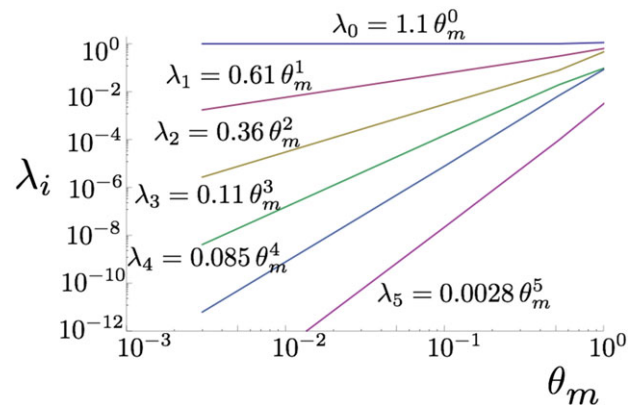

Figure 3 Singular values λ_i, as a function of θ_m.

θ_m. Note that they scale as $\lambda_i \sim \theta_m^i$ as expected. Continuing with the analysis, we show the rotation of $\Delta\mathbf{r}$ onto an orthogonal system $\Delta\tilde{\mathbf{r}}$ in Fig. 4. Note that $\tilde{\zeta}$ is mainly the composition variable ζ, and $\tilde{\tilde{\xi}}$ is mainly the geometry variable ξ. Figure 5 shows the $\overline{U}_2^T$ transformation of the stacks $\tilde{\mathbf{R}}$ onto the rock physics variables $\Delta\tilde{\mathbf{r}}$. Note that the full PP stack is the main contribution to the determination of the composition variable $\tilde{\zeta}$, and the "full" PS stack is the main contribution to the determination of the geometry variable $\tilde{\tilde{\xi}}$. The AVO PP gradient stack is of minor contribution to either, but it is more aligned with $\tilde{\tilde{\xi}}$ and orthogonal to $\tilde{\zeta}$. The fourth-order PP stack R_4 is negligible.

We now increase the maximum angle of incidence to a typical value of $\theta_m = 30°$. The main change is shown in Fig. 6, which shows the $\overline{U}_2^T$ transformation. Although the alignment of the $\tilde{\zeta}$ and the $\tilde{\tilde{\xi}}$ directions stay in the same general directions, they are starting to rotate in the R_0–R_1 plane (full PP and "full" PS), so they are becoming a bit of an admixture of both. Note that the AVO PP stack R_2 and the fourth-order PP stack R_4 still have negligible contribution to both. The reason for this can be seen in the $\overline{\Sigma}_1$ singular values of the $\tilde{\mathbf{R}}$ stacks.
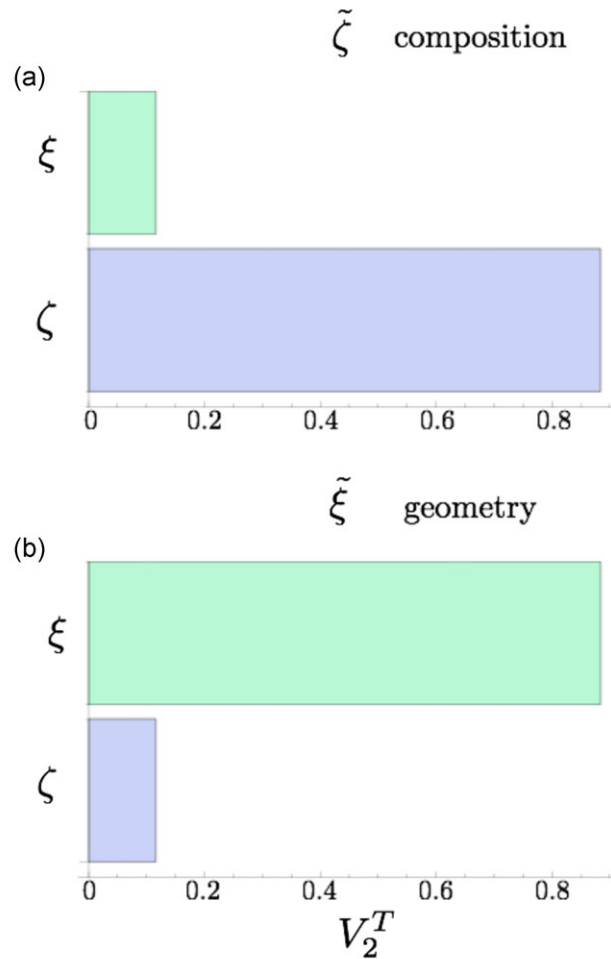

Figure 4 Orthogonal rock physics parameters $\Delta\tilde{\mathbf{r}}$ as given by V_2^T.

The second singular value λ_1 (of the "full" PS stack) is 10 dB less than the first singular value λ_0 (of the full PP stack). The singular value of the AVO PP gradient stack λ_2 is an additional 12 dB less than that of the "full" PS stack, so that it is 22 dB less than that of the full PP stack. It should be noted that the singular value of the fourth-order PP stack λ_4 is 43 dB less than that of the full PP stack. Since the expected SNR of most seismic data is 10 dB to 20 dB, one can reasonably expect to reliably estimate the full PP and the "full" PS stack. It is rather tenuous whether the AVO PP gradient stack can be estimated. There is little probability that the three-term AVO, as determined by the fourth-order PP stack, can be estimated reliably.

Finally, we increase the maximum angle to $\theta = 60°$. This is representative of very long offset AVO data. The main change is shown in Fig. 7, which shows the $\overline{U}_2^T$ transformation. It shows the same modest rotation in the $\tilde{\zeta}$
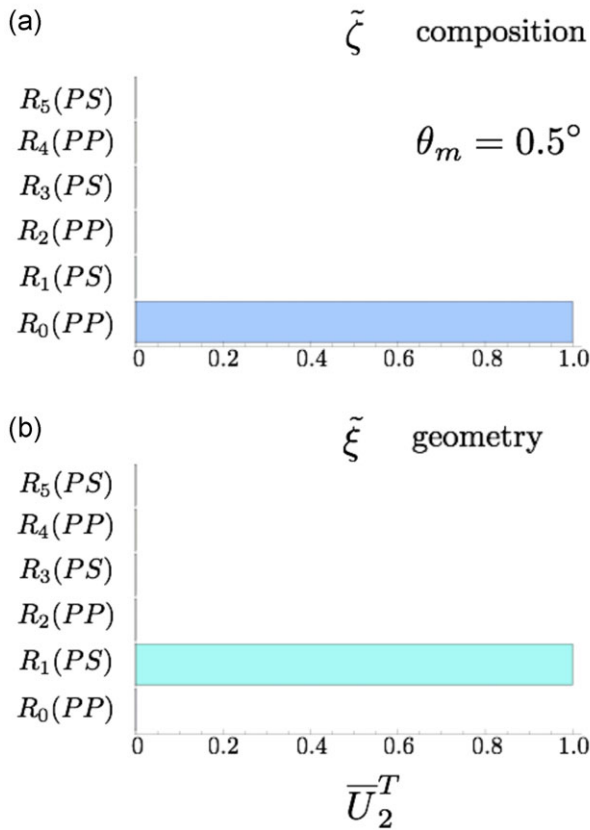
Figure 5 Transformation of the stacks onto the rock physics parameters $\overline{\mathbf{U}}_2^T$ for $\theta_m = 0.5°$.
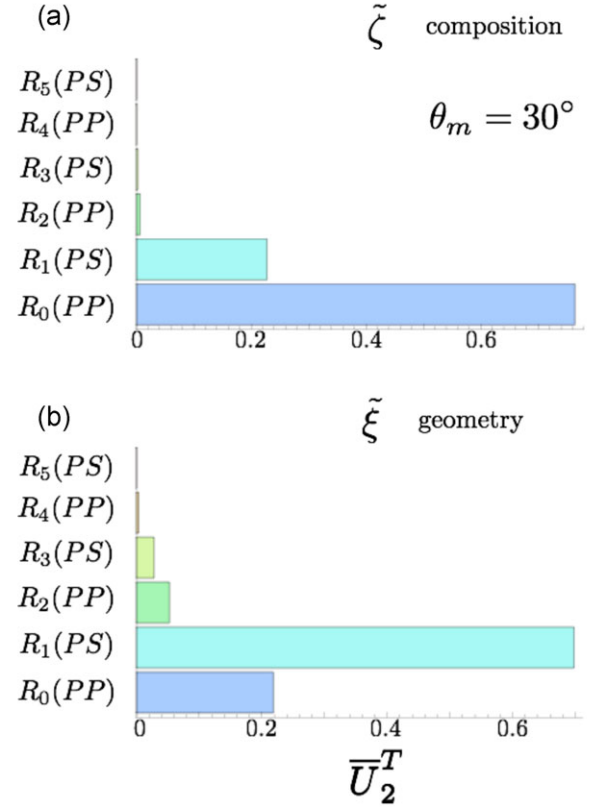

Figure 6 Transformation of the stacks onto the rock physics parameters $\overline{\mathbf{U}}_2^T$ for $\theta_m = 30°$.

and $\tilde{\xi}$ directions as the previous case. The main difference is that the AVO PP gradient stack contributes almost equally with the "full" PS stack to the determination of $\tilde{\xi}$. The reason for this can be seen in the singular values of $\overline{\boldsymbol{\Sigma}}_1$. The singular value of the "full" PS, AVO PP gradient stack, and the fourth-order PP stack are 3 dB, 6 dB, and 20 dB less than the full PP stack, respectively. It is interesting to examine the compound transformation $\overline{\mathbf{U}}_2^T \overline{\mathbf{U}}_1^T$ that defines the two optimal stacks for estimation of the two rock physics parameters $\Delta \tilde{\mathbf{r}}$. They are shown in Fig. 8. The optimal stack weights for the composition $\tilde{\zeta}$ are a difference between the full PP stack and the "full" PS stack. The optimal stack weights for the more important property, i.e., the geometry $\tilde{\xi}$, has roughly equal weights for the "full" PS stack and the far offset PP data.

As we developed earlier, in the theoretical part of the previous section, there is value in examining the relationship between the rock physics and more traditional elastic parameters $\overline{\mathbf{U}}_T^T$. For the rock physics characteristic of the Marcellus shale, the results are shown in Fig. 9. All of the moduli,

whether the bulk, shear, or Young's molulus (i.e., R, G, or E) have roughly equivalent ability to discern the composition $\tilde{\zeta}$. For the geometry $\tilde{\xi}$ however, it is clearly the density ρ, which is the whole story. However, one will need to estimate one of the moduli before the secondary variation (secondary singular value) associated with the density can be understood. We are not advocating inverting for the density. First of all, it is an absolute property and not a relative property such as $\Delta\rho/\rho$. There are grave technical concerns in inverting for such absolute quantities because of the need to incorporate absolute reference values. They are never truly known, and incorporating them in the results will bring bias to the results. Second, it is an unnecessary complication to invert for a meta-parameter and it complicates the incorporation of prior information. Instead, one should invert directly for ξ from a limited number of stacks of $\tilde{\mathbf{R}}$, where the data covariance is diagonal and largest. However, this analysis confims some of the folklore that believes it is density that matters in predicting the performance of unconventional reservoir fracturing.
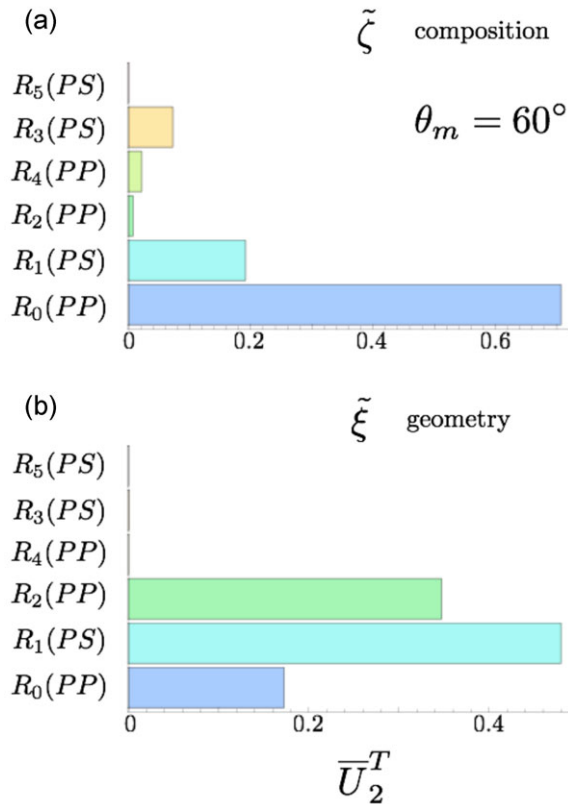
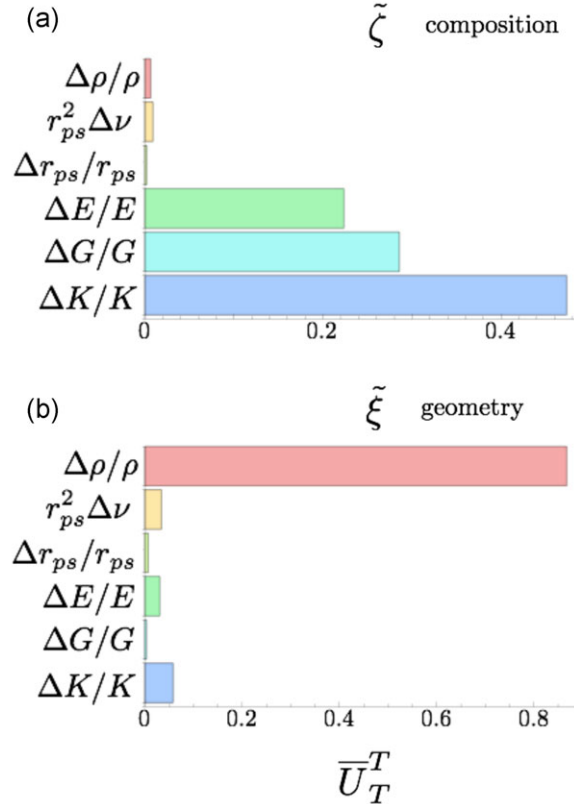**Figure 7** Transformation of the stacks onto the rock physics parameters $\overline{\mathbf{U}}_2^T$ for $\theta_m = 60°$.

Figure 8 Optimal stack weights $\overline{\mathbf{U}}_2^T \overline{\mathbf{U}}_1^T$ as a function of incidence angle θ for the determination of rock physics parameters. First set is for PP data, followed by the weights for PS data. The maximum angle θ_m is 60°.

Detectability with rock physics uncertainty

We now turn our attention to the practical detectability of the rock properties. To do this, we extend the analysis of the Detectability without rock physics uncertainty Section to include the uncertainty in the rock physics $\boldsymbol{\varepsilon}_r$. We use the expression for the five-term A vector given in equation (A29),

Figure 9 Relationship between traditional rock physics parameters and the fundamental rock physics parameters given by $\overline{\mathbf{U}}_T^T$.

a maximum angle of $\theta_m = 60°$, a data error of 1% in reflection coefficient (RFC) units, and base values for the rock physics of $\mathbf{r}_1 = (\zeta_1, \xi_1) = (0.65, 0.79)$ characteristic of the Marcellus shale to be discussed in the following Marcellus prototype model Section. The full probability for $P(\mathbf{r})$ of equation (A26) is shown in Fig. 10. The untruncated width in the $\tilde{\zeta}$ direction is 0.06 and is 0.35 in the $\tilde{\xi}$ direction. The rotation of the ellipsoid is 23°. The dimensions of the ellipsoid is dominated by the rock physics uncertainty for a data error of 1% RFC. The data error becomes as important as the rock physics uncertainty in determining the dimensions of the ellipsoids, if it is increased to 3% RFC.

The contribution of each of the terms in the expression for the reflectivity to the determination of $\tilde{\zeta}$ and $\tilde{\xi}$ is shown in Fig. 11 by the matrix $\overline{\mathbf{U}}_2^T \mathbf{V}_1^T$. The value of $\tilde{\zeta}$ is dominated by $R_0(PP)$ with some contribution from $R_1(PS)$. The value of the important $\tilde{\xi}$ is dominated by $R_1(PS)$ and $R_3(PS)$. This is further clarified by examining the marginal and conditional probabilities for ζ in Fig. 12 and for ξ in Fig. 13. The data that are used (i.e., PP, PP+AVO, PP+PS, or all data) are controlled
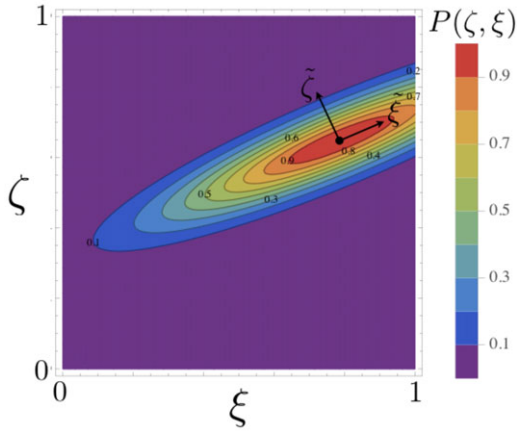
Figure 10 Probability of **r** $P(\zeta, \xi)$ as a function of ζ and ξ. The value of $\mathbf{r}_1$ that is forward modeled is shown as the black dot. The principle directions of the distribution are shown as the black arrows.
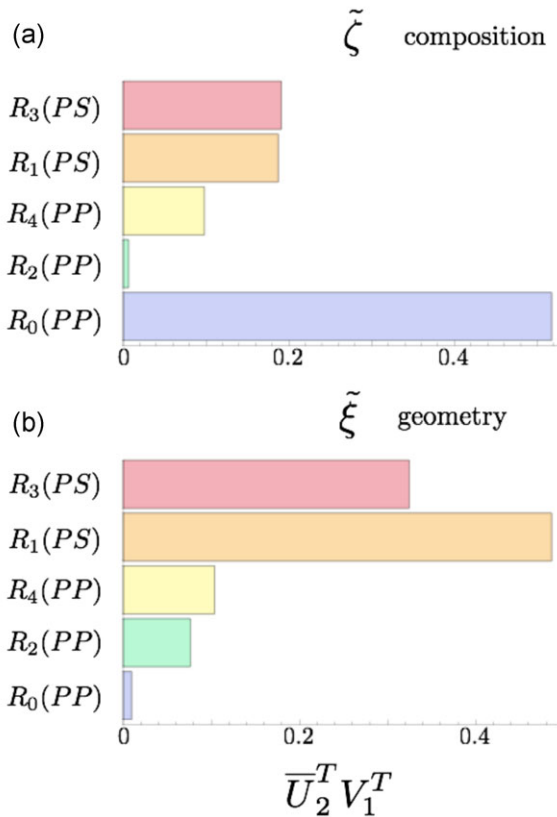

Figure 11 Contribution of each of the stacks to the determination of the principle directions of $P(\zeta, \xi)$. Display of the elements of the matrix $\overline{U}_2^T V_1^T$.
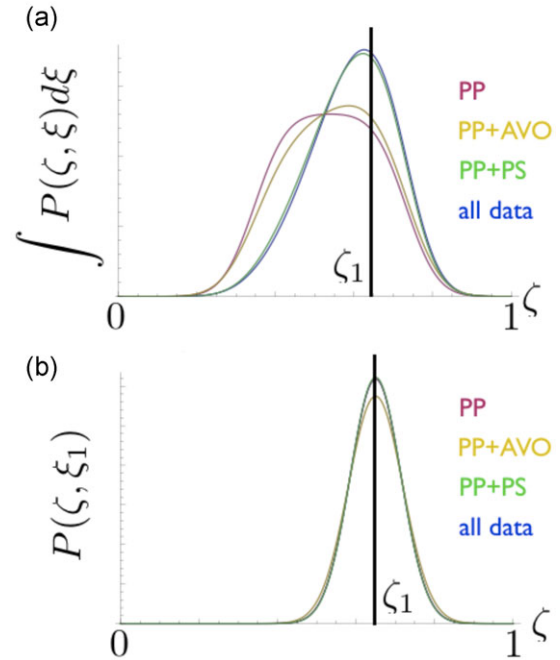

Figure 12 (a) Marginal and (b) conditional probabilities of ζ derived from $P(\zeta, \xi)$. The true values of $\zeta_1 = 0.65$ are shown as black lines. The distribution using the PP data is shown as the magenta line, the PP+AVO data as the yellow line, the PP+PS data as the green line, and all the data as the blue line.

by manipulation of the data covariance $\boldsymbol{\Sigma}_m$ (setting the error to a large value for the data to be excluded). For use of the PP data only, an angle up to $\theta_m = 6°$ is used for the PP data. The marginal probability for ζ is well determined with a standard deviation of about 0.11 for all data sets, but a bias of -0.15 is removed by including the PS data (the standard deviation is also modestly reduced from 0.13 to 0.11). The conditional probability is well determined for all data sets with a standard deviation of 0.06. The marginal probability for ξ is determined with a standard deviation of 0.23, only with the addition of PS data. The conditional probability is well determined for all data types with a modest decrease in the standard deviation from 0.14 to 0.12 with the addition of PS data.

The optimal stack weights for estimation of $\tilde{\zeta}$ and $\tilde{\xi}$, i.e., $\overline{U}_2^T \overline{U}_1^T W_d$, are very similar to those shown in Fig. 8. The first set of weights, that estimate $\tilde{\zeta}$, are roughly a full PP plus a "full" PS stack. The second set of weights, which estimates $\tilde{\xi}$, is a combination of the far offset PS and far offset PP data.

The detectability of the second principle direction $\tilde{\xi}$ is reduced as the maximum angle is decreased to 45°, with very little discrimination remaining for maximum offset angles less than 30°. The implication is that one can not simultaneously determine ζ and ξ, when the incident angle is under 30°. In
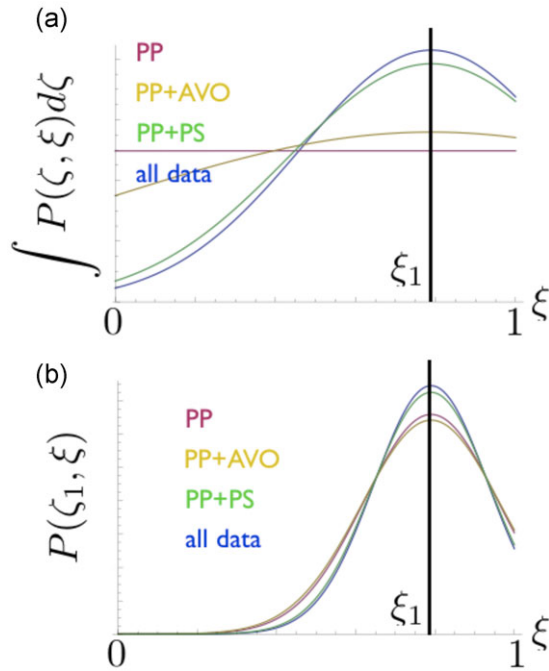
Figure 13 (a) Marginal and (b) conditional probabilities of ξ derived from $P(\zeta, \xi)$. The true values of $\xi_1 = 0.79$ are shown as black lines. The distribution using the PP data is shown as the magenta line, the PP+AVO data as the yellow line, the PP+PS data as the green line, and all the data as the blue line.

order to determine ξ for a small maximum offset angle, the value of ζ must be well constrained. The value of the PS data, in this case, is reduced because the second principle direction is not needed. However, the value of PS data can be preserved in a multiple layer inversion, at more modest maximum offset angles, as will be demonstrated in the Model based inversion Section.

Marcellus prototype model

In order to test the practicality of determining the ductile fraction $f_d = f_{dc}\xi$ and other quantities of interest for an unconventional shale petroleum reservoir, a prototype model of the Marcellus play is constructed. A typical stratigraphic cross section is shown in Fig. 14. Note that the lower Marcellus shale is the primary interval of interest. Typical values of ρ, v_p, and v_s are shown in Fig. 15. Reference lines of the trends in equations (1) and (3) are displayed versus these typical values. The ρ and v_p values are transformed using equations (1) and (5) to give typical ζ and ξ for each layer with the results shown in Fig. 16. Note that the limestones have $\xi \approx 0$, and the marls have $\xi \approx 0.2$. There are two types of shales. One type
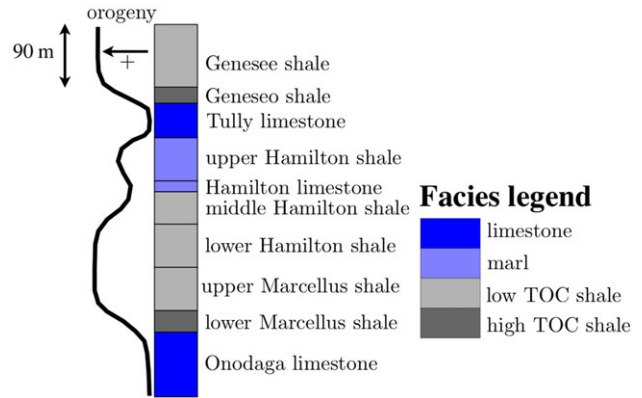

Figure 14 Typical stratigraphic cross section of Marcellus shale play. Shown are two major stratigraphic cycles and one minor cycle.
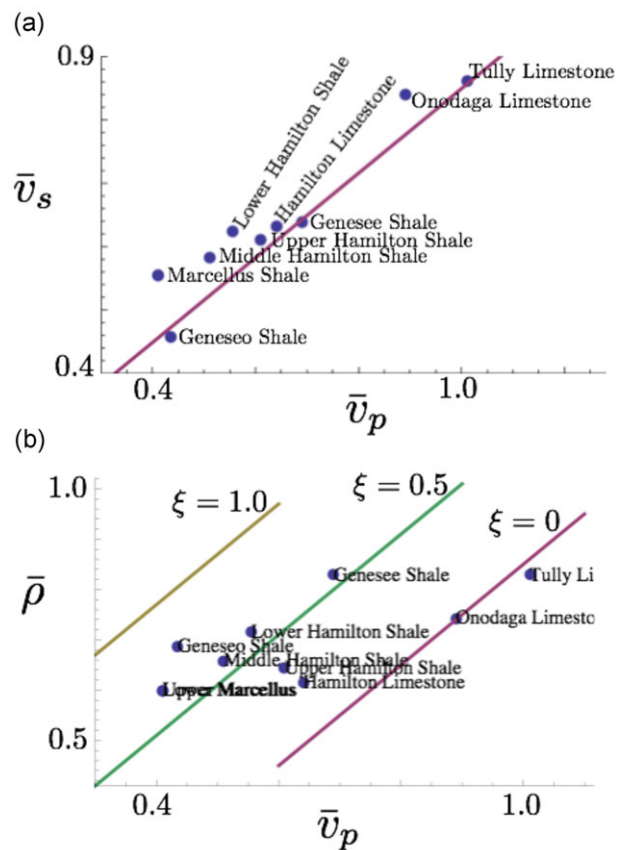

Figure 15 Typical values of ρ, v_p, and v_s for the Marcellus shale play. Values are normalized according to the equation $\bar{x} = (x - x_{min})/(x_{max} - x_{min})$, where min $v_p = 2439$ m/s, max $v_p = 5489$ m/s, min $v_s = 1158$ m/s, max $v_s = 3354$ m/s, min $\rho = 2.1$ g/cc, and max $\rho = 2.8$ g/cc. (a) v_s-v_p values in normalized units. Purple line is the fit trend, equation (3). (b) ρ-v_p values in normalized units. Trend lines of constant ξ, equation (1), are coloured and labelled according to the value of ξ.
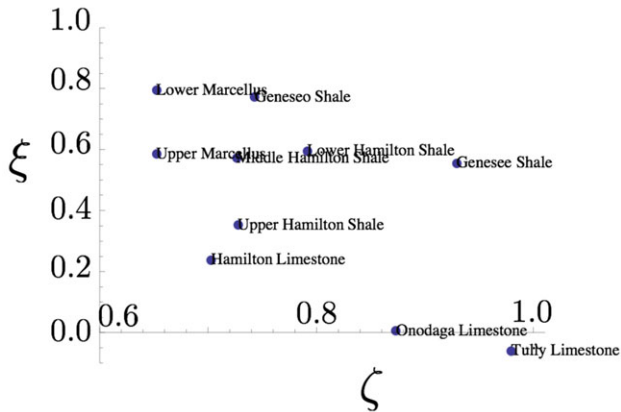
Figure 16 Typical values of ζ and ξ for the Marcellus shale play.
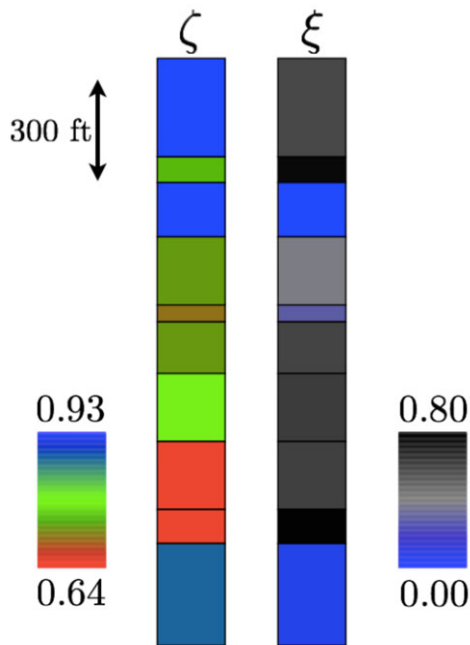

Figure 17 Stratigraphic cross sections with typical values of ζ (i.e., lithology) and ξ (i.e., compaction, diagenesis, or mineral substitution) for the Marcellus shale play.

has $\xi \approx 0.5$, and the other type, the high TOC "frackable" target shales, has $\xi \approx 0.7$. The resulting models for ζ and ξ (where ξ indicates lithology, and ζ indicates compaction, diagenesis, or mineral substitution) are shown in Fig. 17. This is consistent with our earlier identification of ζ with composition and ξ with geometry. Three simplified models, two with two layers, and one with three layers, are shown in Fig. 18. They are constructed to build up to the full model in Fig. 17 in a systematic way. We will first determine what can be learned from the RFC from the bottom and the top of the target layers
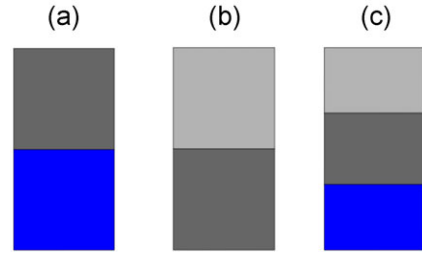

Figure 18 Three simplified models of the Marcellus shale play: (a) high TOC shale on top of a limestone, (b) low TOC shale on top of a high TOC shale, (c) a three layer model of a high TOC shale between a limestone and a low TOC shale.

in Figs. 18a, b. The third model (Fig. 18c) adds the additional information of layer times and the accompanying tuning effects. This is a closer examination of the bottom three layers of the model shown in Fig. 14.

The work of Kohli and Zoback (2013) has shown a strong connection between the ductile fraction and the efficiency of hydraulic fracturing. For this reason, the main focus will be determining the ductile fraction from the converted wave (i.e., cwave or joint PP and PS) surface imaging of the models of Figs. 14 and 18.

It is helpful to understand the geology behind this stratigraphy (Sageman *et al.* 2003). The Marcellus shale and its accompanying stratigraphy was formed in the Devonian time during the tectonic plate collision that formed the Appalachian mountains. The deposition was more specifically associated with the foreland basin caused by the isostatic compensation of the thick crust associated with the collision and uplift. When there was a reduction in the subduction, the sedimentation into the foreland basin was reduced, and the basin became shallow enough to be favorable to carbonate formation. The result was the limestones in the stratigraphic section. When the orogeny recommenced, the basin deepened, but there was a delay in the resumption of the erosion of the mountains and an increase in the sediment load into the foreland basin. This created a good environment for the formation of shales high in organic content. As time progressed, the sediment load resumed, increasing the silt in the shale and lowering its organic content and ductile fraction. This sequence is repeated twice in a significant way in this section and once in a more minor cycle (see the orogeny curve in Fig. 14).

Model-based inversion

It seems difficult to determine the ductile fraction using data with modest maximum angles of incidence θ_m for simple
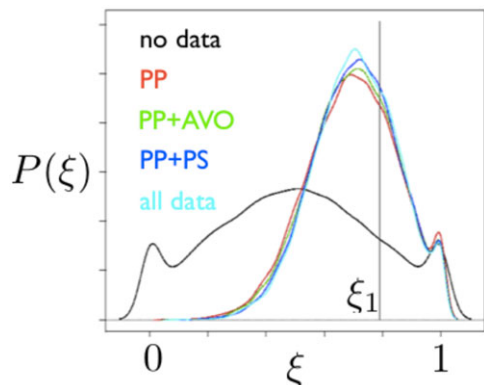
Figure 19 Probability distribution of ξ in the overlying shale layer of the two-layer model shown in Fig. 18a. The value of ξ_1 forward modelled is shown as the black vertical line. The distribution before the use of any seismic data is shown as the black line, after using the PP data is shown as the red line, after using the PP+AVO data as the green line, after using the PP+PS data as the blue line, and after using all the data as the cyan line.

two-layer models, as discussed in the Detectability with rock physics uncertainty Section, and also difficult to evaluate the angle-dependent wavelet effects with the associated angle dependent tuning. The complex model described in the previous Marcellus prototype model Section gives an opportunity to still be successful. There are advantages introduced by the extra data associated with the multiple reflectors (times and reflection strengths), multiple stacks, differential tuning of the different stack bandwidths, and rich prior model assumptions both on the rock physics and on the structure. To demonstrate these advantages, a Bayesian model-based inversion (Gunning and Glinsky 2004; Chen and Glinsky 2014) is done.

To test these ideas, a realistic synthetic seismic forward model of the two layer model of Fig. 18a, and the ten layer model of Fig. 17 is made. The ductile fraction rock physics model of equation (1), equation (3) and equation (5) is used. Uncertainties are assumed to be 25 m on the thicknesses, 3 ms on PP times for the bright reflectors, and 8 ms on PP times for the dim reflectors. No uncertainty in ζ is used although the results are relatively unchanged for uncertainty in ζ less than 0.15. The uncertainty in the ξ value is set to 0.20 except for the limestone layers, which are assumed to have no uncertainty in ξ. The noise on the data stacks is assumed to be 1% RFC with a maximum offset angle of $\theta_m = 45°$.

The results for the two-layer model are shown in Fig. 19, which displays the probability distribution of ξ, i.e., $P(\xi)$, for the overlying shale layer. Note the significant update to the distribution for each seismic data type used and
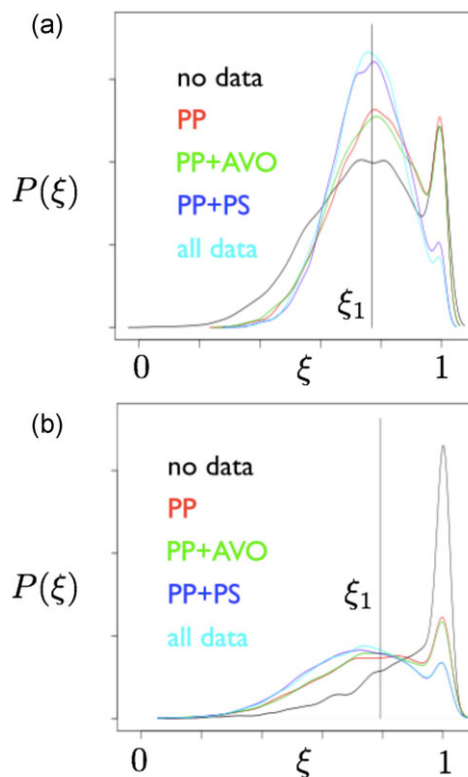

Figure 20 Probability distribution of ξ in the (a) Geneseo shale and (b) lower Marcellus shale of the ten-layer model shown in Fig. 17. The value of ξ_1 forward modelled is shown as the black vertical line. The distribution before the use of any seismic data is shown as the black line, after using the PP data is shown as the red line, after using the PP+AVO data as the green line, after using the PP+PS data as the blue line, and after using all the data as the cyan line.

the very modest improvement with the addition of PS data. Both are consistent with the theoretical result of Fig. 13b. The results become interesting with the additional complexity and information of the ten-layer model. Fig. 20 shows the estimated probability of ductile fraction $P(\xi)$ in the Geneseo shale and the lower Marcellus shale. They represent two situations, one having priors consistent with data (Fig. 20a) and the other having biased priors (Fig. 20b). For the Geneseo layer, without using PS data, the estimated distributions (red and green curves) are bimodal. However, the inclusion of PS data (blue and cyan curves) significantly improves the estimate of ductile fraction, and the unique modes of the posterior distributions correspond to the true value. For the lower Marcellus layer, where the prior is biased to a high value (i.e., $\xi = 1.0$), the use of seismic data generally shifts the distributions towards to the true value, and the inclusion of PS data shifts them much more. The result for the probability distribution
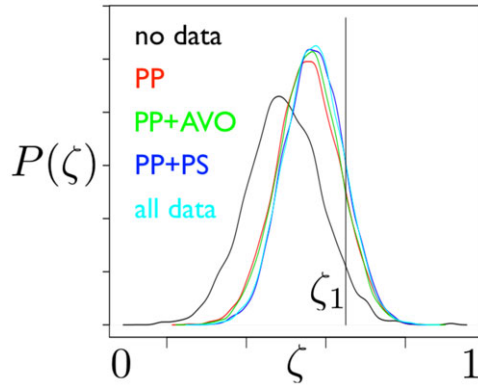
Figure 21 Probability distribution of ζ in the lower Marcellus shale of the ten-layer model shown in Fig. 17. The value of ζ_1 forward modelled is shown as the black vertical line. The distribution before the use of any seismic data is shown as the black line, after using the PP data is shown as the red line, after using the PP+AVO data as the green line, after using the PP+PS data as the blue line, and after using all the data as the cyan line.

of ζ $P(\zeta)$ is shown in Fig. 21. For the lower Marcellus shale, the distribution has a single mode that is moved closer to the true value with the inclusion of the seismic data. There is no improvement by including the AVO or PS data, as expected.

CONCLUSIONS

The purpose of this paper was to establish the underlying fundamentals of quantitative interpretation for unconventional shale reservoirs. This started with the understanding that it is the ductile fraction that controls the geomechancial balance between the rocky road joint friction of the fractures and the viscous joint friction. While this geomechanics was not the subject of this paper, others Zoback *et al.* (2012); Kohli and Zoback (2013) have found sensitive dependence of the dynamic friction on the ductile fraction, resulting to a dramatic change in the fracturing efficiency.

Inspired by this geomechanical observation, we developed and verified, at the mesoscopic level, a rock physics model where the three isotropic elastic properties are only a function of two parameters, i.e., the scaled ductile fraction $\xi = f_d/f_{dc}$, and a composition variable $\zeta = 1 - \exp(-E/E_0)$, which captures compaction, diagenesis, and mineral substitution effects. The first variable captures changes in the geometric microstructure, i.e., how efficient the rock matrix is in supporting stress – modulus per mass or coordination number. The second variable captures the compositional properties of the matrix. It is practically useful that there are only

two parameters and that one of them is directly related to the ductile fraction – the critical parameter for the geomechanics.

The next important question that we answered is how this geometry parameter ξ manifests itself in surface reflection seismic data. The equations relating the rock physics to the reflectivity were all linearized, and an SVD analysis was done to answer this question. The SVD analysis relates the orthogonal components of the seismic reflection data, directly to the fundamental rock properties. The leading order singular value was primarily related to the full PP stack and the composition ζ. The next order singular value was primarily related to the "full" PS stack and the geometry variable $\xi = f_d/f_{dc}$. For reasonable angles of reflection, the higher order stacks, which include the AVO PP gradient stack, all have small SNRs, which would make them hard, if not impossible, to detect. If the angles of incidence could be extended to 60° or more, the AVO PP gradient stack could be substituted for the "full" PS stack because its singular value becomes roughly equal. We wish to emphasize that this is not a three-term AVO analysis to detemine ρ, v_p, and v_s. It is only a two-term analysis for the two rock physics parameters. Because the rock physics only has two parameters, using three stacks creates an over determined system. While using the three stacks would improve the estimates of those two parameters, the third stack is not necessary.

The conclusion is that the PP full stack and the PS "full" (linear weighted with θ or offset) stacks are optimal in the estimation of ζ and ξ, respectively. They are of zeroth and first order in θ, respectively. Conventional AVO "gradient" stacks and large-angle PP response conventionally used to estimate density are of higher order in θ (second and fourth order, respectively). It should be noted that these stacks are average reflectivities or relative quantities. Linear combinations of these two important stacks (normally just the full PP stack for ζ and the "full" PS stack for ξ) are the best "attributes".

A further analysis was done to relate the two fundamental rock physics parameters to traditional elastic parameters. It was found that the composition ζ is primarily related to the moduli (bulk, shear, or Young's), and the geometry $\xi = f_d/f_{dc}$ is primarily related to the density. This is consistent with the common wisdom of the density being needed to predict fracability.

There are two other practical findings of this analysis (as shown in Appendix A). The first is that effective wavelets (for each stack) can be used for the first three stacks (i.e., full PP, "full" PS, and AVO PP gradients). This is because corrections to these wavelets would be of higher order (fourth order in θ_m, compared with the second order accuracy of the reflectivity

calculation). Second, the effect of scale can be captured in renormalization constants that are absorbed into the wavelet normalizations and the effective angle of incidence. These practical findings enable a wavelet derivation process that finds a separate wavelet for each stack and a constant that relates the effective angle of incidence to the true angle of incidence.

The conclusion is that the geophysical forward model is a good approximation for $\theta \to 1$, does not change in form as a function of scale, and allows separation of the wavelet from the reflectivity analysis.

The effect of noise that is a function of the angle of incidence and distortions to the data that are functions of angle of incidence were shown to be corrected by modification of the stack weights (as shown in Appendix B). These weights can be conveniently derived from real data by principle component analysis on the real data. The result is the taper at small and large offsets, and an offset-dependent scalar being applied to the data. This analysis gives theoretical justification to common practices that have been done for more practical reasons.

The final portion of this work focused on the practical application of the theory to both synthetic and to real data. First, the result of determining the stack weights via a principal components analysis on real data was shown. The results support the analytic work and the conclusions of that work. The preliminary SVD analysis was then extended to include rock physics uncertainty and to understand the detectability of ductile fraction. The results support a detectability of ductile fraction using PS data or large offset PP data.

Finally, a set of synthetic models were constructed that are a realistic reproduction of the stratigraphy and rock physics of the Marcellus shale play. These models included uncertainty in the rock physics, angle-dependent wavelet effects, seismic noise, and complex model reflection interference. Both problems induced by these complexities were studied as well as the advantages introduced by multiple extra data associated with the multiple reflectors (times and reflection strength), multiple stacks, differential tuning of the different stack bandwidths, and prior model assumptions. The results confirmed the significant value of multi-component Bayesian inversion (including PS data) and the feasibility of the detection of ductile fraction of the objective shales.

REFERENCES

Bryant S.L., Lerch C. and Glinsky M.E., 2009. Critical grain-size parameters for predicting framework and oating grains in sediments. *Journal of Sedimentary Research* **79**, 817.

Causse E., Riede M., van Wijngaarden A., Buland A., Dutzer J. and Fillon R., 2007a. Amplitude analysis with an optimal model-based linear AVO approximation: Part I - theory. *Geophysics* **72**, C59–C69.

Causse E., Riede M., van Wijngaarden A., Buland A., Dutzer J. and Fillon R., 2007b. Amplitude analysis with an optimal model-based linear AVO approximation: Part II field data example. *Geophysics* **72**, C71–C79.

Chen J. and Glinsky M.E., 2014. Stochastic inversion of seismic PP and PS data for reservoir parameter estimation. Geophysics **72**, R233–R246.

Clarkson C., Solano N., Bustin R., Bustin A., Chalmers G., He L., et al., 2013. Pore structure characterization of north american shale gas reservoirs using usans/sans, gas adsorption, and mercury intrusion. *Fuel* **103**, 606–616.

Demartini D. and Glinsky M.E., 2006. A model for variation of velocity versus density trends in porous sedimentary rocks. *Journal of Apl[lied Physics* **100**, 014910.

Goodway B., Perez M., Varsek J. and Abaco C., 2010. Seismic petrophysics and isotropic-anisotropic AVO methods for unconventional gas exploration. *The Leading Edge* **29**, 1500–1508.

Gunning J. and Glinsky M.E., 2004. Delivery: an open-source model-based Bayesian seismic inversion program. *Computers and Geosciences* **30**, 619–636.

Gunning J. and Glinsky M.E., 2006. Wavelet extractor: A Bayesian well-tie and wavelet extraction program. *Computers and Geosciences* **32**, 681–695.

Gunning J. and Glinsky M.E., 2007. Detection of reservoir quality using Bayesian seismic inversion. *Geophysics* **72**, R37.

Guo Z., Li X.-Y., Liu C., Feng X. and Shen Y., 2013. A shale rock physics model for analysis of brittleness index, mineralogy and porosity in the Barnett shale. *Journal of Geophysics and Engineering* **10**, 025006.

Han D., Nur A. and Morgan D., 1986. Effects of porosity and clay content on wave velocities in sandstones. *Geophysics* **51**, 2093–2107.

Hornby B., Schwartz L. and Hudson J., 1994. Anisotropic effective medium modeling of the elastic properties of shales. *Geophysics* **59**, 1570–1583.

Khadeeva Y. and Vernik L., 2013. Rock physics model for unconventional shales. SEG Technical Program Expanded Abstracts, 2757–2761.

Kohli A.H. and Zoback M.D., 2013. Frictional properties of shale reservoir rocks. *Journal of Geophysical Research: Solid Earth* **118**, 5109–5125.

Maggiore M., 2010. *A modern introduction to quantum field theory*. Oxford University Press.

Mahmoudian F. and Margrave G., 2004. Three parameter AVO inversion with PP and PS data using offset binning: SEG Technical Program, Expanded Abstracts, 240–243.

Pervukhina M., Piane C., Dewhurst D., Clennell M. and Bols H., 2013. An estimation of pore pressure in shales from sonic velocities. SEG Technical Program, Expanded Abstracts, 2653–2658.

Sageman B.B., Murphy A.E., Werne J.P., Straeten C.A.V., Hollander D.J. and Lyons T.W., 2003. A tale of shales: the relative roles

of production, decomposition, and dilution in the accumulation of organic-rich strata, middleupper Devonian, Appalachian basin. *Chemical Geology* **195**, 229–273.

Saleh S. and de Bruin J., 2000. AVO attribute extraction via principal component analysis. SEG Technical Program, Expanded Abstracts, 126–129.

Sayers, C., 2005. Seismic anisotropy of shales. *Geophysical Prospecting* **53**, 667–676.

Sayers C., 2013. The effect of kerogen on the AVO response of organic-rich shales. *The Leading Edge* **32**, 1514–1519.

Shaw R.K. and Sen M.K., 2004. Born integral, stationary phase and linearized reection coefficients in weak anisotropic media. *Geophysical Journal International* **158**, 225–238.

Stauffer D. and Aharony A., 1994. *Introduction to Percolation Theory.* CRC Press.

Stewart R., Gaiser J., Brown R. and Lawton D., 2002. Converted wave seismic exploration: methods. *Geophysics* **67**, 1348–1363.

Varela I., Maultzsch S., Chapman M. and Li X., 2009. Fracture density inversion from a physical geological model using azimuthal AVO with optimal basis functions. SEG Technical Program, Expanded Abstracts, 2075–2079.

Veire H. and Landr M., 2006. Simultaneous inversion of PP and PS seismic data. *Geophysics* **71**, R1–R10.

Vernik L. and Kachanov M., 2010. Modeling elastic properties of siliciclastic rocks. *Geophysics* **75**, E171–E182.

Zoback M.D., Kohli A. and McClure M., 2012. The importance of slow slip on faults during hyrdraulic fracturing stimulation of shale gas reservoirs. Proceedings of the Americas Unconventional Resources Conference, Pittsburg, PA.

APPENDIX A

GEOPHYSICAL FORWARD MODEL

This appendix develops an understanding of both the P-to-P, (R_{PP}), and the P-to-S, (R_{PS}), reflection responses for an isotropic medium. This novel expansion and simplification of the geophysical model facilitates the SVD analysis. The form of the geophysical model enables clear identification of the eigenvalues according to their θ order and a clear interpretation of the eigenvectors of the seismic data as the well-known full PP, "full" PS, and AVO PP "gradient" stacks. The mapping of the eigenvectors of the data to the fundamental rock physics parameters is also clear and simple. Although it may seem that the truncation of the expansion limits the forward model to $\theta \ll 1$, it is not the case. First of all, the more well-known starting expressions that are the result of the eikonal and weak scattering approximations, i.e., equations (A1) and (A2), break down as $\theta \rightarrow 1$. Another manifestation of the pathology of the starting expressions for the geophysical forward model is the inability to renormalize them (averaging the equations at different scale while keeping the form of the equations the same). Physics can not change depending on the scale that it is measured. To correct the pathology, the theory is formally truncated at second order, and renormalization coefficients are introduced that are essentially changes in PP wavelet amplitude, PS wavelet amplitude, and effective incident angle as a function of scale. This theory is well known to be renormalizable. A practical implication and a manifestation of the healthy behavior of this truncated theory is that it can be shown to closely match the full-wave solution at all scales with a suitable choice of the renormalization coefficients as a function of scale. Second, the health of the theory is manifested in the fact that, before the truncation to second order, the constants in front of the θ expansion terms are asymptotically convergent. So although $\theta \rightarrow 1$, the terms in the Taylor expansion still converge asymptotically. Third, the truncated geophysical model allows us to conveniently derive the separate wavelets and renormalization constants by a conventional wavelet derivation process Gunning and Glinsky (2006) using the well logs and corresponding measured seismic data – it allows us to separate the wavelet from the reflectivity analysis to second order in θ.

We start by assuming weak scattering and make both the further assumptions of small contrast (that is, $\Delta\rho/\rho$, $\Delta v_p/v_p$, and $\Delta v_s/v_s \ll 1$) and plane waves (eikonal approximation). The latter is a rather complicated assumption on both the frequency and angle of incidence θ. We shall return to this later in this Appendix. The expressions (Shaw and Sen 2004) for the reflection response will be linear in the contrasts due to the first approximation, with coefficients that are functions of the angle of incidence θ and the ratio of the velocities $r_{sp} \equiv v_s/v_p$:

$$
\begin{aligned}
R_{PP} = {} & \frac{1}{2}\left(\frac{\Delta\rho}{\rho} + \frac{\Delta v_p}{v_p}\right) \\
& + \left(-2 r_{sp}^2 \frac{\Delta\rho}{\rho} + \frac{1}{2}\frac{\Delta v_p}{v_p} - 4 r_{sp}^2 \frac{\Delta v_s}{v_s}\right)\sin^2\theta \\
& + \frac{1}{2}\frac{\Delta v_p}{v_p}\sin^2\theta\tan^2\theta,
\end{aligned}
\tag{A1}
$$

$$
R_{PS} = -\frac{\sin\theta}{\cos\theta_{PS}}\left[\frac{1}{2}\frac{\Delta\rho}{\rho} + \left(\frac{\Delta\rho}{\rho} + 2\frac{\Delta v_s}{v_s}\right)\right.
$$
$$
\left. \left(r_{sp}\cos\theta\cos\theta_{PS} - r_{sp}^2\sin^2\theta\right)\right],
\tag{A2}
$$

where θ_{PS} is the reflected angle of the S wave. Making use of Snell's law:

$$
\frac{\sin\theta_{PS}}{v_s} = \frac{\sin\theta}{v_p},
\tag{A3}
$$

some basic trigonometric identities and combining terms of common order in $\sin\theta$, we can write the reflectivities as:

$$R_{PP} = \frac{1}{2}\left(\frac{\Delta\rho}{\rho} + \frac{\Delta v_p}{v_p}\right)$$
$$+ \left(-2r_{sp}^2\frac{\Delta\rho}{\rho} + \frac{1}{2}\frac{\Delta v_p}{v_p} - 4r_{sp}^2\frac{\Delta v_s}{v_s}\right)\sin^2\theta$$
$$+ \frac{1}{2}\frac{\Delta v_p}{v_p}\frac{\sin^4\theta}{\cos^2\theta}, \quad (A4)$$

$$R_{PS} = \left[\left(-\frac{1}{2} - r_{sp}\right)\frac{\Delta\rho}{\rho} - 2r_{sp}\frac{\Delta v_s}{v_s}\right]\frac{\sin\theta}{\sqrt{1 - (r_{sp}\sin\theta)^2}}$$
$$+ \left[\frac{r_{sp}}{2}(1 + r_{sp})^2\frac{\Delta\rho}{\rho} + r_{sp}(1 + r_{sp})^2\frac{\Delta v_s}{v_s}\right]\frac{\sin^3\theta}{\sqrt{1 - (r_{sp}\sin\theta)^2}}$$
$$+ \left(r_{sp}\frac{\Delta\rho}{\rho} + 2r_{sp}\frac{\Delta v_s}{v_s}\right)\left[\frac{1 - \cos\theta\sqrt{1 - (r_{sp}\sin\theta)^2}}{\sin^2\theta}\right. \quad (A5)$$
$$\left. - \frac{1}{2}(1 + r_{sp}^2)\right]\frac{\sin^3\theta}{\sqrt{1 - (r_{sp}\sin\theta)^2}}.$$

Expanding to the fourth order in θ leads to the expressions

$$R_{PP} = \frac{1}{2}\left(\frac{\Delta\rho}{\rho} + \frac{\Delta v_p}{v_p}\right)$$
$$+ \left(-2r_{sp}^2\frac{\Delta\rho}{\rho} + \frac{1}{2}\frac{\Delta v_p}{v_p} - 4r_{sp}^2\frac{\Delta v_s}{v_s}\right)\theta^2$$
$$+ \left(\frac{2}{3}r_{sp}^2\frac{\Delta\rho}{\rho} + \frac{1}{3}\frac{\Delta v_p}{v_p} + \frac{4}{3}r_{sp}^2\frac{\Delta v_s}{v_s}\right)\theta^4 + \mathcal{O}(\theta^6), \quad (A6)$$

$$R_{PS} = \left[\left(-\frac{1}{2} - r_{sp}\right)\frac{\Delta\rho}{\rho} - 2r_{sp}\frac{\Delta v_s}{v_s}\right]\theta$$
$$+ \left[\left(\frac{1}{12} + \frac{2}{3}r_{sp} + \frac{3}{4}r_{sp}^2\right)\frac{\Delta\rho}{\rho}\right.$$
$$\left. + \left(\frac{4}{3}r_{sp} + 2r_{sp}^2\right)\frac{\Delta v_s}{v_s}\right]\theta^3 + \mathcal{O}(\theta^5). \quad (A7)$$

We have been careful to write these expressions in a bilinear form in terms of the small contrast (i.e., $\Delta\rho/\rho$, $\Delta v_p/v_p$, $\Delta v_s/v_s$) and the angle of incidence (i.e., $\sin^n\theta$ or θ). This will facilitate the SVD analysis. Note that the coefficients of this bilinear transformation are only functions of the dimensionless parameter, r_{sp}.

Before we continue our analysis, we take a closer look at the plane wave (or eikonal) portion of the weak scattering (or Born) approximation. This is a quite non-trivial assumption

that puts an upper limit on the validity of the θ, given by the condition that the dimensionless scale of the perturbation

$$\frac{\lambda}{T\cos\theta} \equiv s \ll 1, \quad (A8)$$

where λ is the wavelength of the wave and T is the scale of the gradient or the thickness of the layer. The problem is that this can never be satisfied because there is no well defined scale for the medium. The question now becomes: how does the expression for R_{PP} and R_{PS} (which we now call

$$R \equiv (R_{PP}; R_{PS}) \quad (A9)$$

collectively), given in the expansions of equation (A6) and equation (A8), average as a function of dimensionless scale, s? We now evoke well-known theoretical physics concepts of renormalization (Maggiore 2010), to recognize that we need to expand in scale about the "ground state" harmonic oscillator. We introduce three running coupling constants $a_0(s)$, $a_1(s)$, and $a_2(s)$ and define the coefficients of the reflectivity, ordered by θ^n as

$$A_0(\Delta\mathbf{c}) = \frac{1}{2}\left(\frac{\Delta\rho}{\rho} + \frac{\Delta v_p}{v_p}\right), \quad (A10)$$

$$A_1(\Delta\mathbf{c}) = -\left(\frac{1}{2} + r_{sp}\right)\frac{\Delta\rho}{\rho} - 2r_{sp}\frac{\Delta v_s}{v_s}, \quad (A11)$$

$$A_2(\Delta\mathbf{c}) = -2r_{sp}^2\frac{\Delta\rho}{\rho} + \frac{1}{2}\frac{\Delta v_p}{v_p} - 4r_{sp}^2\frac{\Delta v_s}{v_s}, \quad (A12)$$

where the small contrasts $\Delta\mathbf{c} \equiv (\Delta\rho/\rho, \Delta v_p/v_p, \Delta v_s/v_s)$ are taken at the same reference scale s. The reflectivity at a scale s, can now be written as

$$R = [a_0 A_0 + a_2 A_2\theta^2; a_1 A_1\theta]. \quad (A13)$$

Another way of looking at this is a redefinition of incidence angle $\bar{\theta} \equiv \theta\sqrt{a_2/a_0}$ and reflection coefficient $\bar{R} \equiv [R_{PP}/a_0; R_{PS}/(a_1\sqrt{a_0/a_2})]$ so that

$$\bar{R} = [A_0 + A_2\bar{\theta}^2; A_1\bar{\theta}]. \quad (A14)$$

The relationship between these expressions is just that of dressed to undressed fields. In the case that there is a well-defined scale and θ is small enough, $a_0 = a_1 = a_2 = 1$. Otherwise, one must calculate the running coupling constants for the scale of interest using a characteristic well log of the isotropic elastic properties and a forward wave solution with a wavelet of scale λ.

Recognizing that we will be truncating the expansion at the second order in θ, we now develop a convenient approximation to the forward model of a spike convolution, i.e.,

$$R(\theta; t) = \sum_k R(\theta; \Delta \mathbf{c}_k) \, W(\theta; t - t_k), \qquad (A15)$$

where $W(\theta; t)$ is a given angle-dependent wavelet and the summation is over the $\{k\}$ contrasts or interfaces. The problem with this expression is the θ dependence of the wavelet. We would like to eliminate it and replace it by average wavelets. To this end, we now decompose $R(\theta; \Delta \mathbf{c})$ according to its θ dependence. Given the simple form of equations (A6) and (A8), it would have three singular values λ_i and singular vectors $\xi_i(\theta)$. For a more general expansion as given in equations, (A4) and (A5), it would have more singular values, $\lambda_i \sim \mathcal{O}(\theta_m^i)$, where θ_m is the maximum angle of incidence. This structure was analyzed in more detail in the Detectability without rock physics uncertainty Section. For now, we just project $R(\theta; t)$ onto this basis

$$R_i(t) \equiv \int \xi_i(\theta) \, R(\theta; t) \, d\theta, \qquad (A16)$$

and define

$$W_i(t) \equiv \int \xi_i(\theta) \, W(\theta; t) \, d\theta, \qquad (A17)$$

$$\Delta W_i(\theta; t) \equiv W(\theta; t) - W_i(t), \qquad (A18)$$

$$R_i(\Delta \mathbf{c}) \equiv \int \xi_i(\theta) \, R(\theta; \Delta \mathbf{c}) \, d\theta, \qquad (A19)$$

$$\Delta R_i(\theta; \Delta \mathbf{c}) \equiv R(\theta; \Delta \mathbf{c}) - R_i(\Delta \mathbf{c}). \qquad (A20)$$

Remember that to second order

$$R(\theta; \Delta \mathbf{c}) = [a_0 A_0(\Delta \mathbf{c}) + a_2 A_2(\Delta \mathbf{c})\theta^2; a_1 A_1(\Delta \mathbf{c})\theta] + \mathcal{O}(\theta^3). \, (A21)$$

Recognizing that

$$\int \xi_i(\theta) \, \Delta W_i(\theta; t) \, d\theta = \int \xi_i(\theta) \, \Delta R_i(\theta; t) \, d\theta = 0 \qquad (A22)$$

and that ΔW_i and ΔR_i are of second order in θ^2, we find that

$$R_i(t) = \sum_k \int d\theta \, \xi_i(\theta) \, [R_i(\Delta \mathbf{c}_k) + \Delta R_i(\theta; \Delta \mathbf{c}_k)]$$
$$[W_i(t - t_k) + \Delta W_i(\theta; t - t_k)] \qquad (A23)$$

$$= \sum_k \left[R_i(\Delta \mathbf{c}_k) \, W_i(t - t_k) \right.$$
$$\left. + \int d\theta \, \xi_i(\theta) \, \Delta R_i(\theta; \Delta \mathbf{c}_k) \, \Delta W_i(\theta; t - t_k) \right] \qquad (A24)$$

$$= \sum_k R_i(\Delta \mathbf{c}_k) \, W_i(t - t_k) + \mathcal{O}(\theta_m^4). \qquad (A25)$$

This is an extremely convenient result. What it allows us to do is to calculate an effective wavelet $W_i(t)$ for each weighted stack $R_i(t)$. We can then form a simple spike convolution forward model using the singular vectors of the reflectivity $R_i(\Delta \mathbf{c})$ for each stack. The order of $R_i(\Delta \mathbf{c})$ will be θ_m^i. We will therefore be able to use this separation of R and W up to the third order in $R_i(\Delta \mathbf{c})$.

For the analysis of of the probability distributions, it is convenient to write the expression for the reflection coefficients $\mathbf{R}_0$ as a compound linear transformation, as shown in equation (10), and explicitly calculate the rock physics covariance matrix $\boldsymbol{\Sigma}_r$. First of all the expression for $\mathbf{R}_0$ contains the product of matrices where

$$\Delta \mathbf{r} \equiv \begin{pmatrix} d\zeta \\ d\xi \end{pmatrix}, \quad \Delta \mathbf{c} \equiv \begin{pmatrix} \frac{\Delta \rho}{\rho} \\ \frac{\Delta v_p}{v_p} \\ \frac{\Delta v_s}{v_s} \end{pmatrix}, \quad \mathbf{A} \equiv \begin{pmatrix} A_0 \\ A_1 \\ A_2 \\ \vdots \end{pmatrix},$$

$$\mathbf{R} = \begin{pmatrix} R_{PP}(\theta = 0) \\ \vdots \\ R_{PP}(\theta_m) \\ R_{PS}(\theta = 0) \\ \vdots \\ R_{PS}(\theta_m) \end{pmatrix}, \qquad (A26)$$

$$\mathbf{R} = \mathbf{M}_\theta \, \mathbf{A}, \quad \mathbf{A} = \mathbf{M}_A \, \Delta \mathbf{c}, \quad \Delta \mathbf{c} = \mathbf{M}_{RP} \, \Delta \mathbf{r}, \text{ and}$$

$$\mathbf{M}_{RP} = \begin{pmatrix} \frac{B_\rho \, B_{vp}}{\rho} & \frac{B_\rho \, C_{vp} + C_\rho}{\rho} \\ \frac{B_{vp}}{v_p} & \frac{C_{vp}}{v_p} \\ \left(\frac{B_{vs}}{r_{sp}}\right) \frac{B_{vp}}{v_p} & \left(\frac{B_{vs}}{r_{sp}}\right) \frac{C_{vp}}{v_p} \end{pmatrix}. \qquad (A27)$$

All of the important physics is contained in the renormalized, second order in θ_m, three-term expressions. For this case,

$$
\mathbf{M}_\theta =
\begin{pmatrix}
1 & 0 & 0 \\
1 & 0 & (\Delta\theta)^2 \\
1 & 0 & (2\Delta\theta)^2 \\
\vdots & \vdots & \vdots \\
1 & 0 & [(N-2)\Delta\theta]^2 \\
1 & 0 & \theta_m^2 \\
0 & 0 & 0 \\
0 & \Delta\theta & 0 \\
0 & 2\Delta\theta & 0 \\
\vdots & \vdots & \vdots \\
0 & (N-2)\Delta\theta & 0 \\
0 & \theta_m & 0
\end{pmatrix},
$$

$$
\mathbf{M}_A =
\begin{pmatrix}
\frac{1}{2} & \frac{1}{2} & 0 \\
-\frac{1}{2}-r_{sp} & 0 & -2r_{sp} \\
-2r_{sp}^2 & \frac{1}{2} & -4r_{sp}^2
\end{pmatrix},
\tag{A28}
$$

here $\Delta\theta \equiv \theta_m/(N-1)$. It can be extended to the fourth-order (5 term) in θ_m to give

$$
\mathbf{M}_\theta =
\begin{pmatrix}
1 & 0 & 0 & 0 & 0 \\
1 & 0 & (\Delta\theta)^2 & 0 & (\Delta\theta)^4 \\
1 & 0 & (2\Delta\theta)^2 & 0 & (2\Delta\theta)^4 \\
\vdots & \vdots & \vdots & \vdots & \vdots \\
1 & 0 & [(N-2)\Delta\theta]^2 & 0 & [(N-2)\Delta\theta]^4 \\
1 & 0 & \theta_m^2 & 0 & \theta_m^4 \\
0 & 0 & 0 & 0 & 0 \\
0 & \Delta\theta & 0 & (\Delta\theta)^3 & 0 \\
0 & 2\Delta\theta & 0 & (2\Delta\theta)^3 & 0 \\
\vdots & \vdots & \vdots & \vdots & \vdots \\
0 & (N-2)\Delta\theta & 0 & [(N-2)\Delta\theta]^3 & 0 \\
0 & \theta_m & 0 & \theta_m^3 & 0
\end{pmatrix},
$$

$$
\mathbf{M}_A =
\begin{pmatrix}
\frac{1}{2} & \frac{1}{2} & 0 \\
-\frac{1}{2}-r_{sp} & 0 & -2r_{sp} \\
-2r_{sp}^2 & \frac{1}{2} & -4r_{sp}^2 \\
\frac{1}{12}+\frac{2}{3}r_{sp}+\frac{3}{4}r_{sp}^2 & 0 & \frac{4}{3}r_{sp}+2r_{sp}^2 \\
\frac{2}{3}r_{sp}^2 & \frac{1}{3} & \frac{4}{3}r_{sp}^2
\end{pmatrix}.
\tag{A29}
$$

We can also give a large θ_m version extended to the fifth order (six term) in $\sin\theta_m$

$$
\mathbf{M}_\theta^T =
$$

$$
\left(
\begin{array}{c|c}
1 & 0 \\ \hline
0 & \dfrac{\sin\theta}{\sqrt{1-(r_{sp}\sin\theta)^2}} \\ \hline
\sin^2\theta & 0 \\ \hline
0 & \dfrac{\sin^3\theta}{\sqrt{1-(r_{sp}\sin\theta)^2}} \\ \hline
\dfrac{\sin^4\theta}{\cos^2\theta} & 0 \\ \hline
0 & \left[\dfrac{1-\cos\theta\sqrt{1-(r_{sp}\sin\theta)^2}}{\sin^2\theta}-\frac{1}{2}(1+r_{sp}^2)\right]\dfrac{\sin^3\theta}{\sqrt{1-(r_{sp}\sin\theta)^2}}
\end{array}
\right),
$$

$$
\mathbf{M}_A =
\begin{pmatrix}
\frac{1}{2} & \frac{1}{2} & 0 \\
-\frac{1}{2}-r_{sp} & 0 & -2r_{sp} \\
-2r_{sp}^2 & \frac{1}{2} & -4r_{sp}^2 \\
\frac{r_{sp}}{2}(1+r_{sp})^2 & 0 & r_{sp}(1+r_{sp})^2 \\
0 & \frac{1}{2} & 0 \\
r_{sp} & 0 & 2r_{sp}
\end{pmatrix}.
\tag{A30}
$$

Each block of the $\mathbf{M}_\theta^T$ matrix is an $1 \times N$ matrix with an element for each discrete θ between 0 and θ_m.

We do note the degeneracy in the $\mathbf{M}_A$ matrix for $r_{sp} = 0$ and 1/2. This only reduces the rank of $\mathbf{M}_A$ to 2 at $r_{sp} = 1/2$. Since $\Delta\mathbf{r}$ is only of dimension 2, there is no loss of sensitivity of $\mathbf{R}$ to $\Delta\mathbf{r}$.

Using equations (1), (3) and (5), the form of the rock physics covariance can be shown to be

$$
\frac{\boldsymbol{\Sigma}_r}{2} =
\begin{pmatrix}
\frac{\sigma_\rho^2+B_\rho^2\sigma_{vp}^2}{\rho^2} & \frac{B_\rho}{\rho v_p}\sigma_{vp}^2 & \frac{B_\rho B_{vs}}{\rho v_s}\sigma_{vp}^2 \\
\frac{B_\rho}{\rho v_p}\sigma_{vp}^2 & \frac{\sigma_{vp}^2}{v_p^2} & \frac{B_{vs}}{v_p v_s}\sigma_{vp}^2 \\
\frac{B_\rho B_{vs}}{\rho v_s}\sigma_{vp}^2 & \frac{B_{vs}}{v_p v_s}\sigma_{vp}^2 & \frac{\sigma_{vs}^2+B_{vs}^2\sigma_{vp}^2}{v_s^2}
\end{pmatrix}.
\tag{A31}
$$

Finally we move on to writing the matrix equations for the geophysical rock properties. The relationship between the geophysical rock properties and $\Delta\mathbf{c}$ is linearized so that

$$
\Delta\mathbf{r}_T = \mathbf{M}_T\Delta\mathbf{c},
\tag{A32}
$$

where

$$
\Delta\mathbf{r}_T \equiv
\begin{pmatrix}
\frac{\Delta K}{K} \\
\frac{\Delta G}{G} \\
\frac{\Delta E}{E} \\
\frac{\Delta r_{ps}}{r_{ps}} \\
r_{ps}^2\,\Delta v \\
\frac{\Delta\rho}{\rho}
\end{pmatrix}, \text{ and}
\tag{A33}
$$

$$\mathbf{M}_T = \begin{pmatrix} 1 & -\frac{6}{4r_{sp}^2-3} & \frac{8r_{sp}^2}{4r_{sp}^2-3} \\ 1 & 0 & 2 \\ 1 & \frac{2r_{sp}^2}{(r_{sp}-1)(r_{sp}+1)\left(4r_{sp}^2-3\right)} & \frac{2\left(2r_{sp}^2-3\right)\left(2r_{sp}^2-1\right)}{(r_{sp}-1)(r_{sp}+1)\left(4r_{sp}^2-3\right)} \\ 0 & 1 & -1 \\ 0 & \frac{1}{(r_{sp}-1)^2(r_{sp}+1)^2} & -\frac{1}{(r_{sp}-1)^2(r_{sp}+1)^2} \\ 1 & 0 & 0 \end{pmatrix}. \qquad (A34)$$

This linear relationship is singular for $r_{sp} = 1$ and $\sqrt{3/4}$. It is constructed to have a well defined limit at $r_{sp} = 0$ of

$$\mathbf{M}_T = \begin{pmatrix} 1 & 2 & 0 \\ 1 & 0 & 2 \\ 1 & -2 & 4 \\ 0 & 1 & -1 \\ 0 & 1 & -1 \\ 1 & 0 & 0 \end{pmatrix}, \qquad (A35)$$

which shows that the moduli (bulk, shear, and Youngs) are mixtures of the density and the velocities, the Poisson ratio and the v_p to v_s ratio are both similar quantities showing correlation in v_p to v_s, and the density is modestly perpendicular to the moduli. These facts are useful in understanding the results shown in Fig. 9 in the Detectability without rock physics uncertainty Section.

APPENDIX B

NOISE AND DATA DISTORTION EFFECT ON STACK WEIGHTS

This appendix examines how noise and systematic data distortions will modify what the optimal stack weights will be. In practice, these weights are determined by a principal components analysis of the seismic data. The renormalization constants $a_i(s)$, the averaged wavelets $W_i(t)$, and the data covariance matrix $\mathbf{\Sigma}_m$, are also determined by the wavelet derivation process (Gunning and Glinsky 2006) at a well location. All of these parameters are estimated by a minimization of synthetic seismic mismatch with an additional estimate of the uncertainty in this minimalization. What we wish to show by this study are reasons for the deviation of the optimal stack weights from the theoretical ones shown earlier in the Detectability without rock physics uncertainty Section.

We start by showing the effect of having more noise on both the near and far offsets. The nominal SNR is chosen to be 25 dB. For simplicity, we have used the three-term expression for $\mathbf{M}_\theta$ and $\mathbf{M}_A$ given in equation (A28). A diagonal form of $\mathbf{W}_d$ is chosen with the diagonal elements shown in Fig. B1a. The effect on the stack weights $\overline{\mathbf{U}}_1^T \mathbf{W}_d$
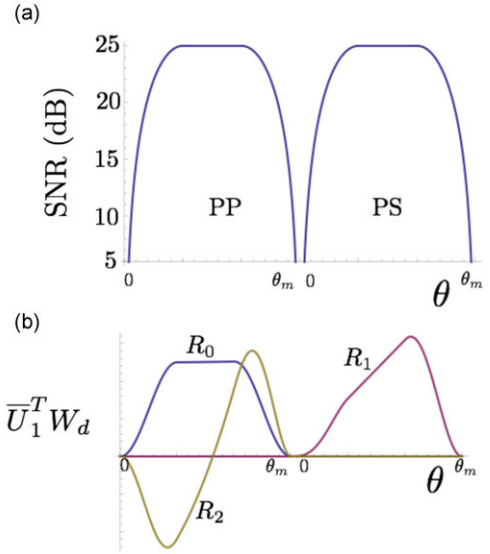

Figure B1 Effect of angle-dependent noise on stack weights. (a) More noise is assumed on the near and far offsets as shown by the SNR $\mathbf{W}_d$ as a function of angle. (b) Stack weights $\overline{\mathbf{U}}_1^T \mathbf{W}_d$ as a function of incident angle θ for the PP and PS data.
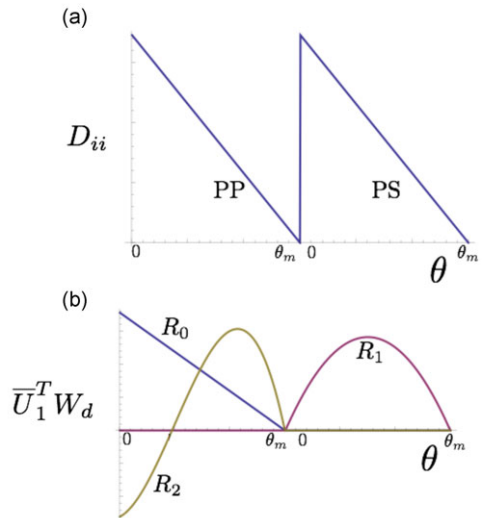

Figure B2 Effect of angle-dependent distortion on stack weights, with a constant SNR. (a) "Hot nears" such that the near offset traces are artificially enhanced is shown by the offset dependent distortion D_{ii} as a function of angle. (b) Stack weights $\overline{\mathbf{U}}_1^T \mathbf{W}_d$ as a function of incident angle θ for the PP and PS data.

are shown in Fig. B1b. They display a common taper that is traditionally applied to weighted stacks at small and large offsets. This analysis gives a possible physical origin for such a taper. Such tapers are also found by the principal components analysis discussed in the previous paragraph and the analysis
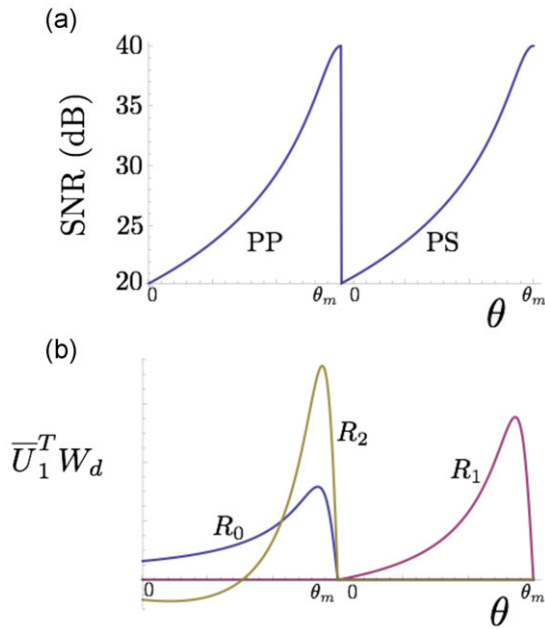
Figure B3 Effect of angle-dependent distortion on stack weights, which is applied after the noise. Angle-dependent distortion is the same as that in Fig. B2. (a) SNR as a function of angle. (b) Stack weights $\overline{U}_1^T W_d$ as a function of incident angle θ for the PP and PS data.

to be shown in Appendix C. The singular values of the stacks $\overline{\Sigma}_1$ are 23 dB, 12 dB, and -2 dB for the the full PP, "full" PS, and the AVO PP gradient stacks, respectively. The same SNR was assumed for both the PP and PS stacks. If the SNR was smaller for the PS. it would only change the relative weight of the PS reflectivity, not the shape of the weights.

We now simulate another common data non-ideality – "hot nears", which is an offset-dependent distortion diagonal **D**, such that the near offset traces are artificially enhanced (see Fig. B2a). If the SNR after this distortion is a constant 25 dB, the stack weights $\overline{U}_1^T W_d$ are shown in Figure B2b. The effect is counterintuitive. Since the far offsets have been multiplied by a smaller number, one might expect them to have a larger weight in the stack to compensate. Instead, they have a smaller weight. This is because they have a decreased amount of signal with the same noise. Hence, the effective SNR is less, and hence the weight is less. The SNR for the three stacks are 25 dB, 9 dB, and -3 dB, respectively.

Next we assume the same "hot nears" of the previous case, but now we assume that the offset-dependent scalar is applied after the noise so that the noise level is decreased along with signal. We limit the SNR to 40 dB. The same offset-dependent weights shown in Fig. B2a are used. The SNR is modified from a constant 25 dB to that shown in Fig.

B3a. The stack weights $\overline{U}_1^T W_d$ for this case are shown in Fig. B3b. This result is much more intuitive. The larger offsets are weighted more to compensate for the smaller multiplicative constant. This results in the SNR of the second and third stacks to be increased. The resulting SNRs are 24 dB, 13 dB, and 1 dB, respectively.

APPENDIX C

PRINCIPAL COMPONENT ANALYSIS OF STACK WEIGHTS OF REAL DATA

The results of the Detectability without rock physics uncertainty Section demonstrated what the theoretical stack weights should be and Appendix B demonstrated how
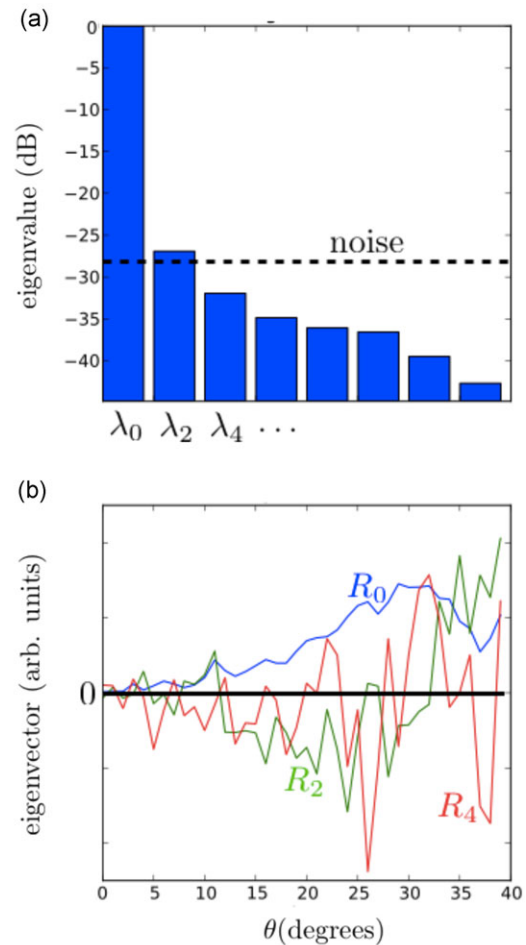

Figure C1 Results of principal components analysis on real data. (a) Eigenvalues displayed in power. Shown as the dotted line is the noise level as estimated from the form of the eigenvectors. (b) three leading eigenvectors.

angle-dependent noise and angle-dependent distortions would affect those weights. Practically, this can be determined from the data. For some real data characteristic of an unconventional shale petroleum reservoir, such an analysis was done on PP data.

A standard principle components analysis was done on the covariance matrix constructed from 12 separate samples of an angle gather. Each sample has a basis of 40 angles (0 to $40°$). The covariance matrix is 40×40, and it characterizes at the variance structure of the amplitudes for the 40 angles estimated from our 12 samples. The eigenvalues and eigenvectors of the covariance matrix are calculated numerically for this square symmetric matrix. The eigenvalues, or principle components, are proportional to the variance of data associated with the respective eigenvectors.

The results of this analysis are shown in Fig. C1. The first eigenvector (labelled as R_0 in Fig. C1b) is smaller than expected for small angles (it should be a constant). As we have shown in the previous section, this could be because the data have more noise at small angles or because of "hot nears" as displayed in Figs. B1 and B3, respectively. We do not know which of these two is the true cause, but we do not need to know. We just need to form the stacks with these derived weights and proceed with the wavelet derivation process and the rest of the analysis. The second eigenvector R_2 shows rough characteristics of an AVO PP gradient stack, which is far offsets minus the near offsets. It does show a large amount of oscillations that have the properties of noise. This demonstrates that the signal is roughly the same size as the noise. The third eigenvector R_4 looks like only noise. This is highlighted in Fig. C1a, which shows the eigenvalues in reference the the noise level implied by these eigenvectors.

The analysis was continued, and a Bayesian wavelet derivation (Gunning and Glinsky 2006) was done using a method that estimated the noise using the well log. The results showed a good match of the synthetic to the seismic and a reasonable wavelet (close to zero phase with a main lobe and two smaller side lobes). More importantly, when the noise level was compared with the size of the dominate reflections, we determined that the SNR was about 20 dB. This compares to the 28 dB estimated from the principle components analysis.